

Investigating the Nested Structure of the Outflow from the Low Luminosity Protostar IRAS 16253-2429 using JWST and ALMA

MAYANK NARANG[†] ,¹ HIMANSHU TYAGI ,² NAGAYOSHI OHASHI ,³ P. MANOJ ,² S. THOMAS MEGEATH ,⁴
 JOHN J. TOBIN ,⁵ EWINE F. VAN DISHOECK ,^{6,7} NEAL J. EVANS II ,⁸ DAN M. WATSON ,⁹
 ALESSIO CARATTI O GARATTI ,¹⁰ JES K. JØRGENSEN ,¹¹ ROBERT GUTERMUTH ,¹² YUSUKE ASO ,^{13,14}
 HENRIK BEUTHER ,¹⁵ LESLIE W. LOONEY ,^{16,5} DAVID A. NEUFELD ,¹⁷ GUILLEM ANGLADA ,¹⁸ MAYRA OSORIO ,¹⁸
 ADAM E. RUBINSTEIN ,⁹ SAMUEL FEDERMAN ,^{4,10} LEE W. HARTMANN ,¹⁹ POONEH NAZARI ,⁶
 NICOLE KARNATH ,^{20,21} HENDRIK LINZ ,^{15,22} THOMAS STANKE ,⁷ TYLER L. BOURKE ,²³ YAO-LUN YANG ,²⁴
 ROLF KUIPER,²⁵ JOEL GREEN ,²⁶ PAMELA KLAASSEN ,²⁷ WAFA ZAKRI ,²⁸ NOLAN HABEL ,²⁹
 NASHANTY BRUNKEN ,⁶ JAMES MUZEROLLE ,²⁶ KATERINA SLAVICINSKA ,⁶ AMELIA M. STUTZ ,³⁰
 LUKASZ TYCHONIEC ,⁶ SCOTT WOLK ,²¹ WILL R. M. ROCHA ,⁶ AND WILLIAM J. FISCHER ,²⁶

¹ Academia Sinica Institute of Astronomy and Astrophysics, 11F Astronomy-Mathematics Building, AS/NTU, No. 1, Sec. 4, Roosevelt Rd, Taipei 106216, Taiwan*

² Department of Astronomy and Astrophysics Tata Institute of Fundamental Research

Homi Bhabha Road, Colaba, Mumbai 400005, India

³ Academia Sinica Institute of Astronomy and Astrophysics, 11F of Astronomy-Mathematics Building, AS/NTU, No. 1, Sec. 4, Roosevelt Rd, Taipei 106216, Taiwan

⁴ Ritter Astrophysical Research Center, Department of Physics and Astronomy, University of Toledo, Toledo, OH 43606, USA

⁵ National Radio Astronomy Observatory, 520 Edgemont Rd., Charlottesville, VA 22903 USA

⁶ Leiden Observatory, Universiteit Leiden, Leiden, Zuid-Holland, NL

⁷ Max-Planck Institut für Extraterrestrische Physik, Garching bei München, DE

⁸ Department of Astronomy, The University of Texas at Austin, 2515 Speedway, Stop C1400, Austin, Texas 78712-1205, USA

⁹ University of Rochester, Rochester, NY, US

¹⁰ INAF-Osservatorio Astronomico di Capodimonte, IT

¹¹ Niels Bohr Institute, University of Copenhagen, Øster Voldgade 5-7, 1350, Copenhagen, Denmark

¹² University of Massachusetts Amherst, Amherst, MA, US

¹³ Korea Astronomy and Space Science Institute, 776 Daedeok-daero, Yuseong-gu, Daejeon 34055, Republic of Korea

¹⁴ Division of Astronomy and Space Science, University of Science and Technology, 217 Gajeong-ro, Yuseong-gu, Daejeon 34113, Republic of Korea

¹⁵ Max Planck Institute for Astronomy, Heidelberg, Baden Wuerttemberg, DE

¹⁶ Department of Astronomy, University of Illinois, 1002 West Green St, Urbana, IL 61801, USA

¹⁷ William H. Miller III Department of Physics and Astronomy, The Johns Hopkins University, Baltimore, MD, USA

¹⁸ Instituto de Astrofísica de Andalucía, CSIC, Glorieta de la Astronomía s/n, E-18008 Granada, ES

¹⁹ Department of Astronomy, University of Michigan – Ann Arbor, Ann Arbor, MI 48109, USA

²⁰ Space Science Institute, Boulder, CO, US

²¹ Center for Astrophysics Harvard & Smithsonian, Cambridge, MA, US

²² Friedrich-Schiller-Universität, Jena, Thüringen, DE

²³ SKA Observatory, Jodrell Bank, Lower Withington, Macclesfield SK11 9FT, UK

²⁴ RIKEN Cluster for Pioneering Research, Wako-shi, Saitama, 351-0106, Japan

²⁵ Faculty of Physics, University of Duisburg-Essen, Lotharstraße 1, D-47057 Duisburg, Germany

²⁶ Space Telescope Science Institute, 3700 San Martin Drive, Baltimore, MD 21218, US

²⁷ United Kingdom Astronomy Technology Centre, Edinburgh, GB

²⁸ Physical Sciences Department, Jazan University, Jazan, Saudi Arabia

²⁹ Jet Propulsion Laboratory, California Institute of Technology, 4800 Oak Grove Drive, Pasadena, CA 91109, USA

³⁰ Departamento de Astronomía, Universidad de Concepción, Casilla 160-C, Concepción, Chile

ABSTRACT

Understanding the earliest stage of star and planet formation requires detailed observations to address the connection and interplay between the accretion, outflow and disk evolution. We present results from the observations of the low luminosity ($L_{\text{bol}} \sim 0.2 L_{\odot}$) and mass ($M_* \sim 0.15 M_{\odot}$) Class 0 protostar IRAS 16253–2429, conducted as part of the *eDisk* ALMA large program and the JWST cycle-1 GO program *IPA*. Observations reveal a wide hourglass-shaped continuum cavity traced in scattered light (at $\leq 5 \mu\text{m}$), with a brighter, extended northern side. We detect 15 pure rotational H_2 transitions (E_{up} : 1015–21411 K), revealing a wide-angle molecular outflow. The outflow width (as traced in H_2 0-0 S(11)) at the protostellar location measures ≤ 35 au, slightly larger than the dust and Keplerian disk diameters (~ 30 au) but wider than the 20–23 au jet width in [Fe II]. The opening angle narrows from 40–35° for the low- J H_2 lines (up to S(5)) and the cold gas component (ALMA ^{12}CO) to ~ 28 –19° for the high- J H_2 lines (S(7)–S(11)). Position-velocity diagrams of H_2 reveal higher velocities for higher E_{up} , ranging from 12.5 km s^{-1} for H_2 0-0 S(1) and S(2) to 28.5 km s^{-1} for H_2 0-0 S(5) and S(7) with respect to the mean flow velocity. The nested excitation and velocity structure of the collimated jet and wide angle wind suggest a magnetohydrodynamic wind as a likely launching mechanism, similar to the findings in other protostars and Class II sources. The lower velocity mm CO may be gas from the infalling envelope accelerated outwards by the wide angle wind along the cavity walls.

1. INTRODUCTION

The process of star formation is governed by the complex interplay between infall, accretion, and feedback mechanisms, which determine the final mass of the star and the initial conditions for planet formation (Dunham et al. 2014; Federrath et al. 2014; Guszejnov et al. 2018, 2022; Fischer et al. 2023; Hsieh et al. 2023; Tobin & Sheehan 2024; Hennebelle & Grudić 2024). During the primary accretion phase (which includes most Class 0 and many Class I objects), protostars amass the bulk of their material due to high accretion rates (e.g., Watson et al. 2016; Manoj et al. 2016; Fischer et al. 2017; Federman et al. 2023; Narang et al. 2023). It is also during the primary accretion phase that the protostellar disk is formed, and the initial conditions of planet formation are set (Tobin & Sheehan 2024).

Protostars, regardless of their mass (spanning three orders of magnitude), share a common structural blueprint (Beltrán & de Wit 2016; Tobin & Sheehan 2024), featuring a central protostar surrounded by a dense infalling envelope of gas and dust, and a circumstellar disk. Collimated jets and wide-angle winds are also launched from the disk that carves cavities into the envelope, launching outflows of entrained gas and reducing the mass available to the nascent protostar (Lee 2020; Ray & Ferreira 2021; Habel et al. 2021; Hsieh et al. 2023; Shang et al. 2023b; Dunham et al. 2024). At the same time these jets and winds remove angular momentum from the disk, thereby driving accretion onto

the central protostar (e.g., Shang et al. 2007; Hartmann et al. 2016; Pudritz & Ray 2019; Ray & Ferreira 2021; Tabone et al. 2022).

Among the various proposed mechanisms for launching outflows, disk winds and X-winds are considered to be the leading contenders. Disk wind models have a characteristic nested velocity structure, where more collimated flows exhibit higher velocities (e.g., Pudritz & Norman 1983, 1986; Shu et al. 1994; Cabrit et al. 1999; Shang et al. 2007; de Valon et al. 2022; Pascucci et al. 2023; Oliva & Kuiper 2023; Feeney-Johansson et al. 2025). JWST observations of protostars and Class II disks also appear to find such nested outflows in atomic and H_2 emission from YSOs (e.g., Pascucci et al. 2025; Caratti o Garatti et al. 2024; Delabrosse et al. 2024; Tychoniec et al. 2024; Narang et al., in prep; Tyagi et al., in prep); but also see Narang et al. (2025). In contrast, X-winds have a similar velocity for the collimated and wide (opening) angle component, although recent models of X-winds generate a slower, wide angle component of shock compressed wind (Shang et al. 2020, 2023a). Recently Nakatani et al. (2025) have demonstrated that photoevaporative wind models can also reproduce several key properties of the observed H_2 winds, such as their nested morphology and overall flux levels; however, these models generally underpredict the high- J emission associated with more spatially extended H_2 structures.

A distinctive feature of disk winds is that they originate across a broad range of disk radii, from the inner disk regions around ~ 0.1 au to several 10s of au (Pudritz & Norman 1983, 1986; Wardle & Koenigl 1993; Konigl & Pudritz 2000; Pudritz et al. 2007; Wang et al. 2019; Pascucci et al. 2023; Oliva & Kuiper 2023), with

* † Currently postdoctoral fellow at Jet Propulsion Laboratory, California Institute of Technology

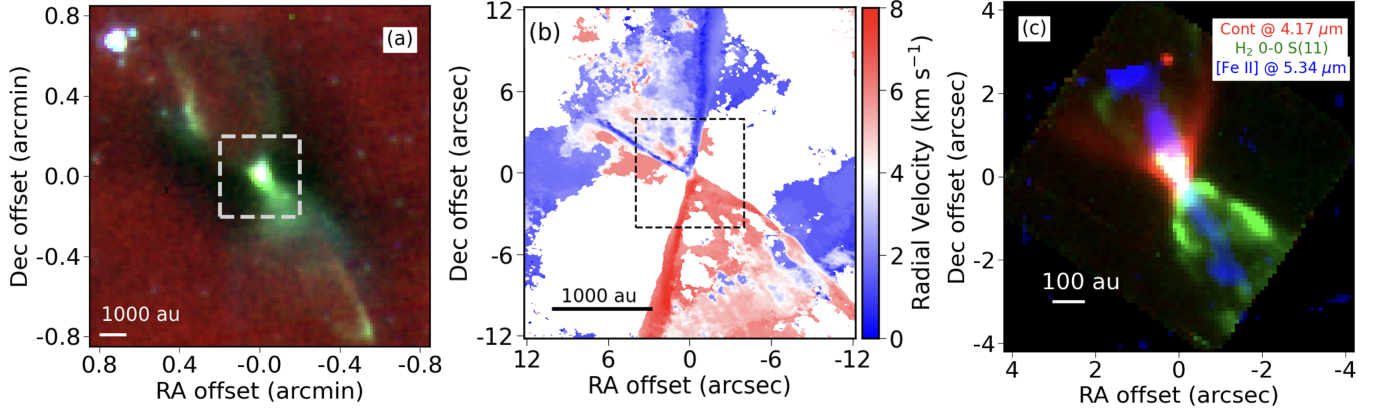


Figure 1. (a) The Spitzer IRAC three color (IRAC 3.6, 4.5 and 8 μm are red, green, and blue, respectively) image of the IRAS 16253–2429 field. The field of view is $\sim 0.8' \times 0.8'$. The dashed gray square outlines the $\sim 24'' \times 24''$ field corresponding to the ALMA FOV in panel b. (b) Moment 1 (velocity) maps in the ^{12}CO $J = 2 - 1$ (robust = 2) line from the ALMA eDisks observations. The dashed back square in the center outlines the $\sim 8'' \times 8''$ field centered on the JWST observations. (c) A zoomed-in view of the NIRSpec and MIRI channel-1 Short (A) field with the red representing continuum emission at 4.17 μm , the green showing H_2 0-0 S(11) at 4.18 μm and the blue depicting [Fe II] at 5.34 μm . A scale bar is given on the bottom left corner for each of the images.

velocities ranging from a few km s^{-1} to several tens of km s^{-1} . In contrast, X-winds are launched when stellar magnetic field lines connect with the disk at the co-rotation radius (around ~ 0.1 au), generating fast ($\sim 100 \text{ km s}^{-1}$) MHD winds that spread widely (e.g., Shu et al. 1994; Shang et al. 2007; Pascucci et al. 2023). Another class of models to explain the outflows from protostars is the jet-driven bow-shock (e.g., Masson & Chernin 1993; Raga & Cabrit 1993; Ostriker et al. 2001; Rabenahary et al. 2022). In this scenario, the jet propagates into the surrounding cloud and forms bow shocks that accelerate and push the ambient gas, producing outflow shells surrounding the jet. Models invoking a pulsed jet create internal working surfaces in the jets that may entrain and accelerate gas inside the cavity, which may appear similar to a disk wind (Rabenahary et al. 2022; Rivera-Ortiz et al. 2023).

In this study, we examine the outflow of IRAS 16253–2429, a Class 0 protostar in the nearby Ophiuchus molecular cloud (Khanzadyan et al. 2004; Stanke et al. 2006). The protostar has a bolometric luminosity of only $\sim 0.2 L_\odot$ and a bolometric temperature of 42 K (eHOPS database¹; Pokhrel et al. 2023; also see Ohashi et al. 2023). At a distance of only ~ 140 pc (adopted from Zucker et al. 2020), IRAS 16253–2429 is the lowest luminosity source in the IPA sample (Federman et al. 2024) and provides an excellent opportunity to study the jet, outflow, and cavity morphology for a class of (very) low-mass protostars in great spatial detail (~ 28

au) (Narang et al. 2024; Federman et al. 2024). Such low luminosity protostars may represent progenitors of very low-mass stars or substellar objects (close to the hydrogen-burning limit) stars very early in the accretion history, and/or low-mass protostars undergoing a quiescent phase (Young et al. 2004; Bourke et al. 2005, 2006; Huard et al. 2006; Dunham et al. 2006; di Francesco et al. 2007; Dunham et al. 2008).

IRAS 16253-2429 has been extensively studied in the (sub)mm wavelength regime (Stanke et al. 2006; Tobin et al. 2011; Hsieh et al. 2016; Yen et al. 2017; Hsieh et al. 2019; Aso et al. 2023; Sharma et al. 2025; Feeney-Johansson et al. 2025). The single dish observations from IRAM-30 telescope and APEX telescope (Hsieh et al. 2016) have shown the CO outflow to be much larger than even the Spitzer IRAC emission spanning up to $\sim 3'$ (~ 0.12 pc) on the southern side.

Recently, IRAS 16253–2429 was observed at high angular resolution ($\sim 0.^{\prime\prime}07$ or 9.8 au for the 1.3 mm continuum) by the ‘Early Planet Formation in Embedded Disks eDisk’ ALMA large program (Ohashi et al. 2023; Aso et al. 2023). These observations revealed a central protostar with a compact disk and a bipolar outflow detected in ^{12}CO $J = 2 - 1$ (Figure 1b). The blue-shifted emission is in the north-east lobe while the red-shifted emission is in the south-west lobe.

The disk is resolved in the dust continuum at 1.3 mm. Similar to Yen et al. (2024) we define the dust disk radius as the 2σ width of the major axis of the deconvolved 2D Gaussian function fitted to the 1.3 mm continuum image. The 2σ width of the major axis from fitting the 1.3 mm ALMA observations is 107 ± 2 mas. At the

¹ <https://irsa.ipac.caltech.edu/data/Herschel/eHOPS/overview.html>

distance of IRAS 16253–2429, this corresponds to a dust disk radius (2σ) of ~ 15 au. The disk mass, assuming an optically thin 1.3 mm dust continuum with a gas-to-dust mass ratio of 100, a disk temperature ranging between 20 and 27 K and different dust opacities, falls within the range of 1.4 to $2.1 \times 10^{-3} M_{\odot}$ (Aso et al. 2023). The inclination angle of 64° , was estimated based on disk fitting (Aso et al. 2023), which is consistent with the inclination angle between 60° – 65° derived based on the modeling CO outflow by Yen et al. (2017).

Aso et al. (2023) also detected a Keplerian gas disk in ^{12}CO with a radius of 16 ± 3 au, similar to the dust disk as measured by the 1.3 mm continuum. By fitting the Keplerian rotation curve, Aso et al. (2023) estimated the dynamical mass of the protostar to be in the range of 0.12 – $0.17 M_{\odot}$. This means that IRAS 16253–2429 is forming a low-mass star and not a brown dwarf, contrary to previous speculations (Hsieh et al. 2016).

The Spitzer Infrared Array Camera (IRAC) images of the source reveal a bipolar hourglass structure in the Northeast to Southwest direction (Figure 1a). This hourglass structure traces the outflow cavities, along with shock features from the flow. Barsony et al. (2010) carried out spectral scan mapping of the protostar using the Spitzer IRS, detecting six pure rotational H_2 lines (0-0 S(2) to 0-0 S(7)). However no fine structure lines were detected from the protostar with Spitzer/IRS.

Recent observations of IRAS 16253-2429 using the JWST Near Infrared Spectrograph (NIRSpec) integral field unit (IFU) and the Mid-Infrared Instrument (MIRI) Medium Resolution Spectrometer (MRS) (Federman et al. 2024; Narang et al. 2024) found that the bipolar hourglass-like structure (due to which the protostar gets its moniker of "wasp-waist" nebula) extends within the inner $7''$ and is traced in both scattered light as well as molecular H_2 lines (Figure 1c). IRAS 16253–2429 also drives a bipolar jet seen in [Fe II], Br- α , and [Ne II] (Federman et al. 2024; Narang et al. 2024). The MIRI MRS spectra of IRAS 16253-2429 shows weak H_2O but strong OH, indicating that H_2O is being photodissociated by UV photons from accretion shocks. Using the production rate of OH we can thus derive an accretion rate. The accretion rate derived from the OH lines is $\dot{M}_{\text{acc}} = 3 \pm 2.2 \times 10^{-10} M_{\odot} \text{ yr}^{-1}$ (Watson et al. 2025). The mass loss rate (based on the atomic jet) is $\leq 1.1 \times 10^{-10} M_{\odot} \text{ yr}^{-1}$ (Narang et al. 2024). Given the low mass accretion/ejection rates, the protostar appears to be going through a quiescent phase where the luminosity is dominated by the intrinsic luminosity of the central protostar. Yet it is driving a highly collimated atomic jet.

In this work, we present the results from joint JWST and ALMA observations of IRAS 16253-2429. The combination of ALMA and JWST is vital for understanding the morphology, kinematics, and excitation conditions in these low luminosity/mass stars, which could not have been done previously. In section 2, we provide a brief overview of observations as well as the data reduction. Our results are reported in section 3, and discussed in detail in section 4. We summarize our findings in section 5.

2. OBSERVATION AND DATA REDUCTION

2.1. JWST Observations

IRAS 16253–2429 was observed as part of the JWST cycle-1 GO proposal Investigating Protostellar Accretion (IPA) (Program ID 1802, PI Tom Megeath; Megeath et al. 2021, Narang et al. 2024; Federman et al. 2024, Rubinstein et al. 2024; Neufeld et al. 2024; Slavickinska et al. 2024; Brunken et al. 2024; Tyagi et al. 2024; Federman et al. 2026). The main goal of the JWST observations was to perform spectral imaging by combining Integral Field Unit spectra of the Mid-Infrared Instrument (MIRI) Medium Resolution Spectroscopy (MRS) (Rieke et al. 2015; Wright et al. 2015, 2023; Law et al. 2024) and the Near Infrared Spectrograph (NIRSpec) (Jakobsen et al. 2022; Böker et al. 2022) from 2.87 to $28 \mu\text{m}$, covering the inner $5.^{\prime\prime}7$ to $14.^{\prime\prime}6$ region of the protostar at a resolution of $\sim 0.^{\prime\prime}2$ (~ 28 au) to $\sim 1''$ (~ 140 au). The NIRSpec IFU and MIRI MRS observations were carried out nearly simultaneously. IRAS 16253–2429 was observed with a pointing center at RA = 16h28m21.62s and Dec = $-24^{\circ}36'24.16''$ based on the 0.87 mm continuum peak from ALMA observations by Hsieh et al. (2019) (see Table 1 for the observation log and Narang et al. 2024).

For the NIRSpec IFU, we used the F290LP/G395M filter/grating combination and for MIRI we used all four channels in the MIRI Medium Resolution Spectroscopy (MRS) IFU mode. We mapped the protostar using a 2×2 mosaic with 10% overlap and the 4-point dither mode. A dedicated background with a similar observation setup (configurations and integration time) $118''$ away from the target was also taken shortly after the observation for MIRI MRS.

To reduce NIRSpec IFU data, we used the JWST pipeline version 1.9.5.dev7+gbf7d3c9b (Bushouse et al. 2023a) and the JWST Calibration References Data System context version jwst_1069.pmap. Details of the NIRSpec data reduction and the custom flagging routine are provided in (Federman et al. 2024). The MIRI MRS data reduction was carried out using the JWST pipeline version 1.11.3 (Bushouse et al. 2023b) and the

Table 1. JWST and ALMA Observations

JWST				
Observation	RA*	Dec*	Start UT	End UT
NIRSpec IRAS 16253-2429	16h28m21.62s	-24d36m24.16s	Jul 22, 2022 15:09:15	Jul 22, 2022 17:59:43
MIRI IRAS 16253-2429	16h28m21.62s	-24d36m24.16s	Jul 23, 2022 04:04:41	Jul 23, 2022 09:58:57
MIRI background	16h28m27.76s	-24d37m46.95s	Jul 23, 2022 10:02:33	Jul 23, 2022 11:35:19
ALMA				
Projected baseline range	RA*	Dec*	Date	
52–10540 m	16h28m21.60s	-24d36m23.40s	2021 October 5, 26, 27, & 28	
14–1290 m	16h28m21.60s	-24d36m23.40s	2022 June 14 & 15	

NOTE—* The observations are centered at these coordinates.

JWST Calibration References Data System context version jwst_1105.pmap (see Narang et al. 2024 for further details). Upon examining the dedicated background IFU observation, we detected diffuse emission from the H₂ S(1) and H₂ S(2) molecular lines; therefore we also created data cubes without subtracting the dedicated background and used those for the analysis.

We further refined the astrometry of our JWST observations, by aligning the MIRI parallel image (from the MIRI imager) to Gaia using Spitzer as an intermediary (see Federman et al. 2024, for details). This alignment between Gaia and the MIRI image carries an astrometric uncertainty of $\sigma_{\text{RA(Gaia-MIRI)}} = 0.^{\circ}05$ and $\sigma_{\text{Dec(Gaia-MIRI)}} = 0.^{\circ}04$. We then correct the MIRI MRS observations using the MIRI parallel images. The NIRSpec IFU astrometry is then corrected using the overlapping spectral range between MIRI MRS and NIRSpec IFU.

2.2. ALMA Observations

IRAS 16253–2429 was observed with ALMA in Cycle 8 using the C-8 (with projected baseline lengths spanning from 52 to 10540 m) and C-5 (with projected baseline lengths ranging from 14 to 1290 m) antenna configurations as part of the ALMA large program ‘Early Planet Formation in Embedded Disks’ (eDisk) (2019.1.00261.L, 2019.A.00034.S) (Ohashi et al. 2023). The observations included CO ($J = 2 - 1$) isotopologues, SO ($J_N = 6_5 - 5_4$), and other molecular lines, observed with Frequency Division Mode (FDM). Additionally, the 1.3 mm continuum emission was obtained from the line-free channels of the spectral windows, with a maximum window width of 1.875 GHz (see also Ohashi et al. 2023 and Aso et al. 2023). The continuum image has a spatial resolution of $0.073'' \times 0.048''$ for a robust factor of 0. For

the ¹²CO emission a velocity resolution of 0.32 km s^{-1} at a angular resolution of $0.^{\circ}17 \times 0.^{\circ}13$ was achieved with a robust factor of 0.5.

3. RESULTS

3.1. Spectra towards the central source

The near-simultaneous observations of IRAS 16253–2429 allowed for the combination of the MIRI MRS and NIRSpec IFU data to produce the complete spectrum of the target from $2.87 \mu\text{m}$ to $28 \mu\text{m}$. We extracted the spectrum from the MIRI MRS 14 μm continuum position (see section 4.1) using an extraction aperture with a radius of $1''$. In Figure 2, we show the complete spectrum from IRAS 16253–2429. We detect several molecular H₂ lines, atomic and fine-structure lines, and the Brackett α (Br α) HI line. While the H₂ lines trace the warm gas in the cavity from the protostar (Figure 1c; also see Federman et al. 2024), the fine structure lines of [Fe II] and [Ne II] along with the Br α line trace a highly collimated, fast jet (Narang et al. 2024, also see Figure 1c.)

In the 4–5 μm range of NIRSpec and MIRI channel-1 short, several CO fundamental rotation-vibration $v = 1 - 0$ R and P branch emission lines with $J \leq 40$ are detected from the central region. These rotation-vibration CO lines may trace parts of the outflow from IRAS 16253–2429 (Rubinstein et al. 2024). We also detect CO₂ fundamental rotation-vibration lines in emission in the gas-phase (around 15 μm). On a careful investigation of the spectra from the protostellar position, we also detected pure rotational transitions of OH in emission with the $^2\Pi_{3/2}$ and $^2\Pi_{1/2}$ electronic configurations in the $\lambda = 10 - 24 \mu\text{m}$ range. We also detect very weak signatures of H₂O emission in the $\lambda = 5 - 7 \mu\text{m}$

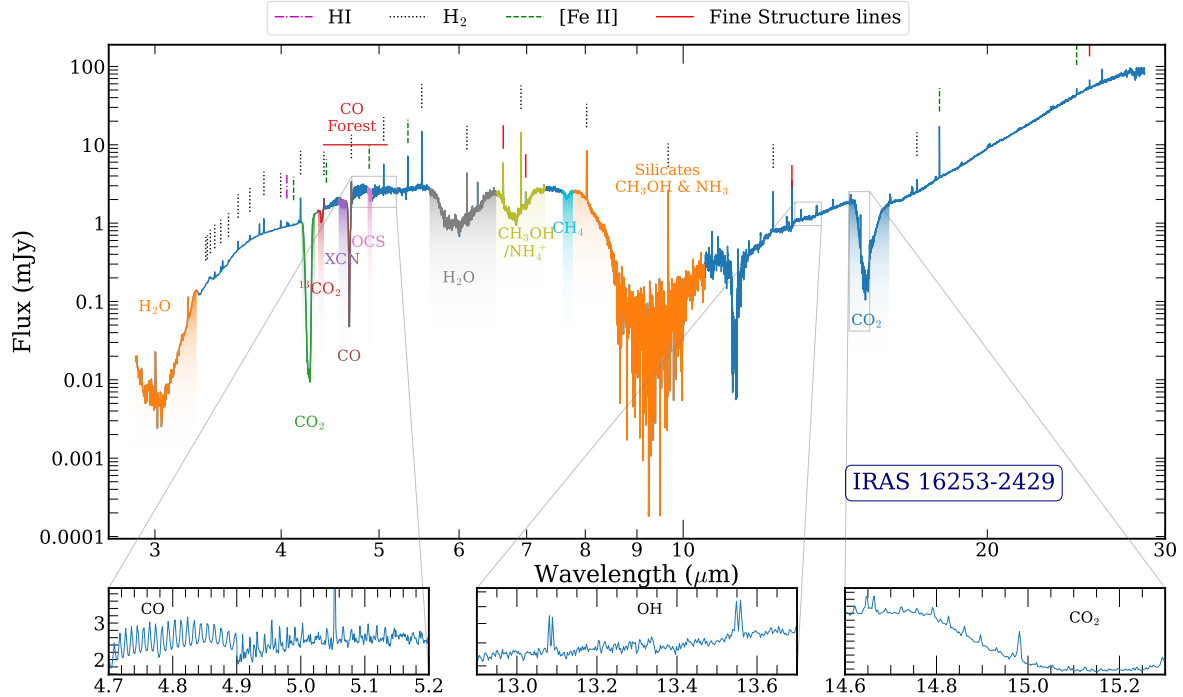


Figure 2. The MIRI MRS and NIRSpec IFU complete spectrum from $2.87 \mu\text{m}$ to $28 \mu\text{m}$ extracted from the ALMA continuum position with an aperture radius of $1''$ centered at the $14 \mu\text{m}$ protostellar position. The offset plots show the zoomed-in view of some of the prominent molecular gas lines detected in IRAS 16253-2429.

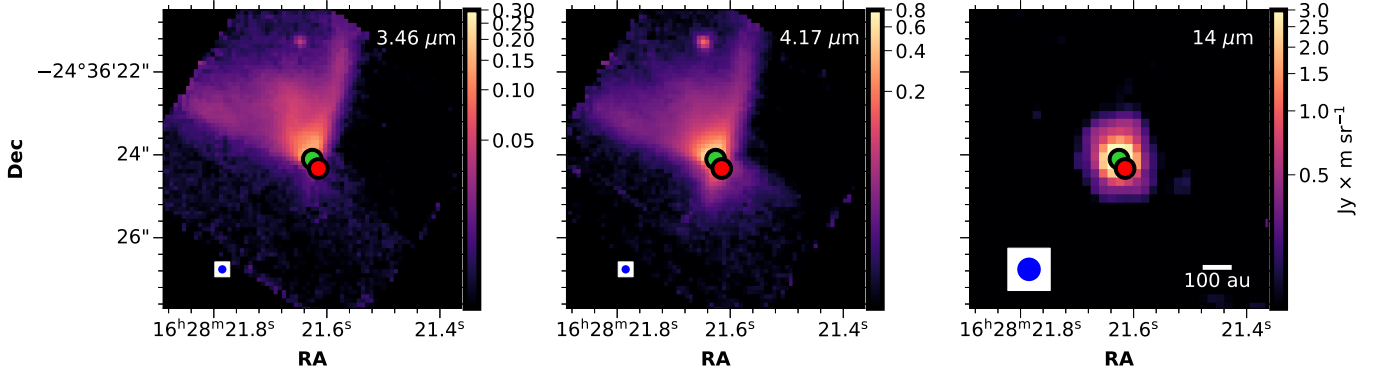


Figure 3. The continuum morphology of IRAS 16253-2429 as a function of wavelength from NIRSpec IFU and MIRI MRS. All images are cropped to the same spatial scale. The green marker is the MRS $14 \mu\text{m}$ position, while the ALMA $1.3 \mu\text{m}$ position is shown as the red marker. A scale bar corresponding to 100 au is shown in the bottom right corner, while the beam size is shown in the bottom left corner as the blue circle.

range leading (Watson et al. 2025) to propose that much of the H_2O in the innermost region of IRAS 16253-2429 has been photodissociated into OH. In addition to gas lines, we detected various ice species, identified in Figure 2 using Table 1 in Boogert et al. 2015. Further details regarding the ice properties and modeling around

IRAS 16253-2429 can be found in Brunken et al. (2024); Nazari et al. (2024).

3.2. Scattered Light and Thermal Continuum

JWST observations of IRAS 16253-2429 reveal ionic jets, molecular wide-angle outflows, and outflow cavity structures down to a spatial resolution of 28 au (with NIRSpec IFU). The collimated jet from the system has

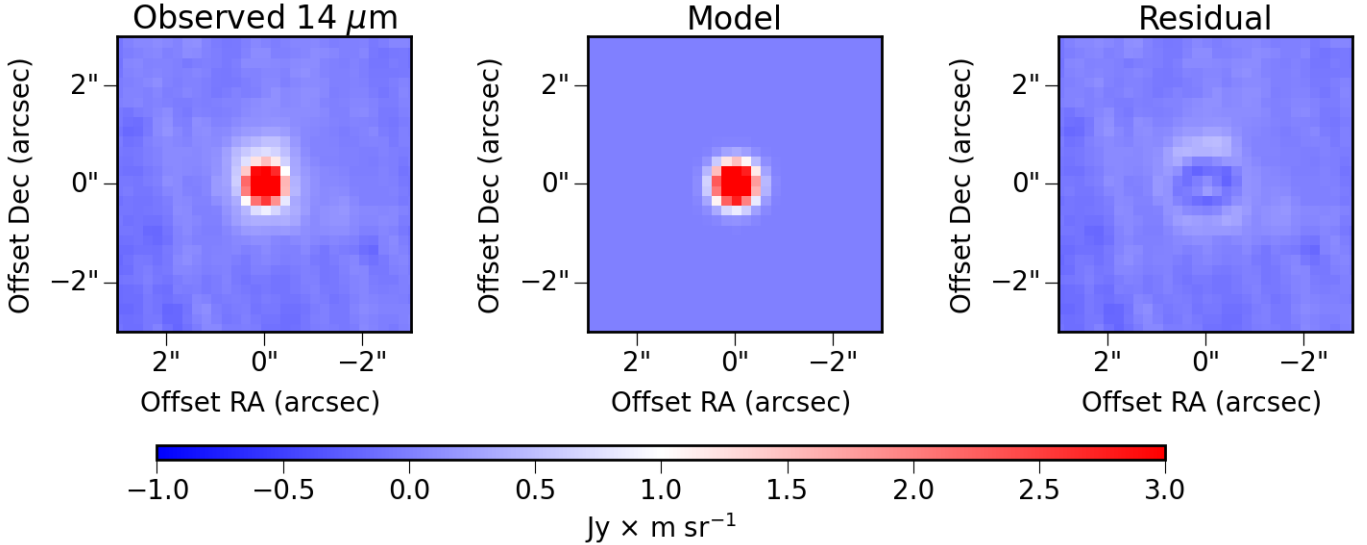


Figure 4. (left) The observed $14\ \mu\text{m}$ image, (center) the best-fit model and (right) the residual. All the three images are on the same spatial and intensity scale.

been extensively studied in [Narang et al. \(2024\)](#) and [Federman et al. \(2024\)](#); thus in this work we will focus on the cavity and molecular outflow morphology and their relationship to the disk and cavity morphology revealed by ALMA.

In Figure 3, we compare the continuum morphology of IRAS 16253–2429 across the NIRSpec IFU and MIRI MRS range at $3.46\ \mu\text{m}$, $4.17\ \mu\text{m}$ and $14\ \mu\text{m}$. For the $14\ \mu\text{m}$ we have subtracted the median flux from the image to account for telescope background. In the NIRSpec wavelength, the continuum traces the cavity in the scattered light and has a wide hourglass-like morphology (also see [Federman et al. 2024](#)). The continuum cavity is brighter on the northern side and extends further as compared to the southern side, consistent with the northern side (containing the blue-shifted outflow) being tilted towards us, this results in less extinction and more forward scattering ([Habel et al. 2021](#)). This is consistent with the higher extinction value found for the southern side of the protostellar cavity by [Narang et al. \(2024\)](#). At longer wavelengths within the NIRSpec range, the southern cavity becomes increasingly visible due to reduced extinction.

At MIRI MRS wavelength $\gtrsim 6\ \mu\text{m}$, the continuum appears nearly as a point source. This can be attributed to the reduced scattering efficiency of dust grains in the mid-infrared ([Pontoppidan et al. 2024](#)) in combination with the reduced sensitivity of the MRS observations compared to the NIRSpec IFU observations. We fit the JWST $14\ \mu\text{m}$ continuum image using a 2D Gaussian to determine the protostellar position. The 2D Gaussian has an FWHM of $0.647''$, which is slightly larger than the theoretical FWHM of $\sim 0.57''$ from [Law](#)

[et al. \(2023\)](#), suggesting that the source is marginally extended even at $14\ \mu\text{m}$. The fit is shown in Figure 4. The JWST $14\ \mu\text{m}$ continuum position is $16^h28^m21.626^s - 24^d36^m24.105^s$, while the ALMA position from [Aso et al. \(2023\)](#) is $16^h28^m21.615^s - 24^d36^m24.33^s$.

We observe an offset of $\sim 0.''27$ (38 au) ($\Delta\text{RA} = \text{RA}_{\text{JWST}} - \text{RA}_{\text{ALMA}} \sim 0.''15$ and $\Delta\text{Dec} = \text{Dec}_{\text{JWST}} - \text{Dec}_{\text{ALMA}} \sim 0.''22$) between the JWST $14\ \mu\text{m}$ continuum position and the ALMA 1.3 mm continuum position along the direction of the blueshifted jet; the offset is more than 3-4 times the estimated astrometric uncertainty of $0.064''$ ([Federman et al. 2024](#)). We further note that the ALMA continuum disk lies where the [Fe II] jet is narrowest (see Figure 9). Even after correcting for the pointing offset for our IFU observations, this offset persists.

Similar positional shifts ($\leq 1''$) between the positions of the outflow driving source at short wavelengths (optical/IR) and long wavelengths (cm/mm) have also been detected previously in other sources (e.g., HL Tau, HH 30, SVS13: [Weintraub et al. 1995](#); [Ray et al. 1996](#); [Diaz-Rodriguez et al. 2022](#)). [Diaz-Rodriguez et al. \(2022\)](#) argued that these positional offsets could be due to the scattered light and thermal emission from illuminated, heated outflow cavity walls being detected while the central protostar is obscured. This effect tends to shift the short wavelength position in the direction of the blue-shifted lobe of the outflow (i.e., shifts the position toward the edge of the cavity closest to the observer, where the jet emerges outward from the cloud). This is similar to what we find in IRAS 16253-2429, as the IR position is displaced to the NE of the position of the embedded protostar (traced by the mm emission) along the

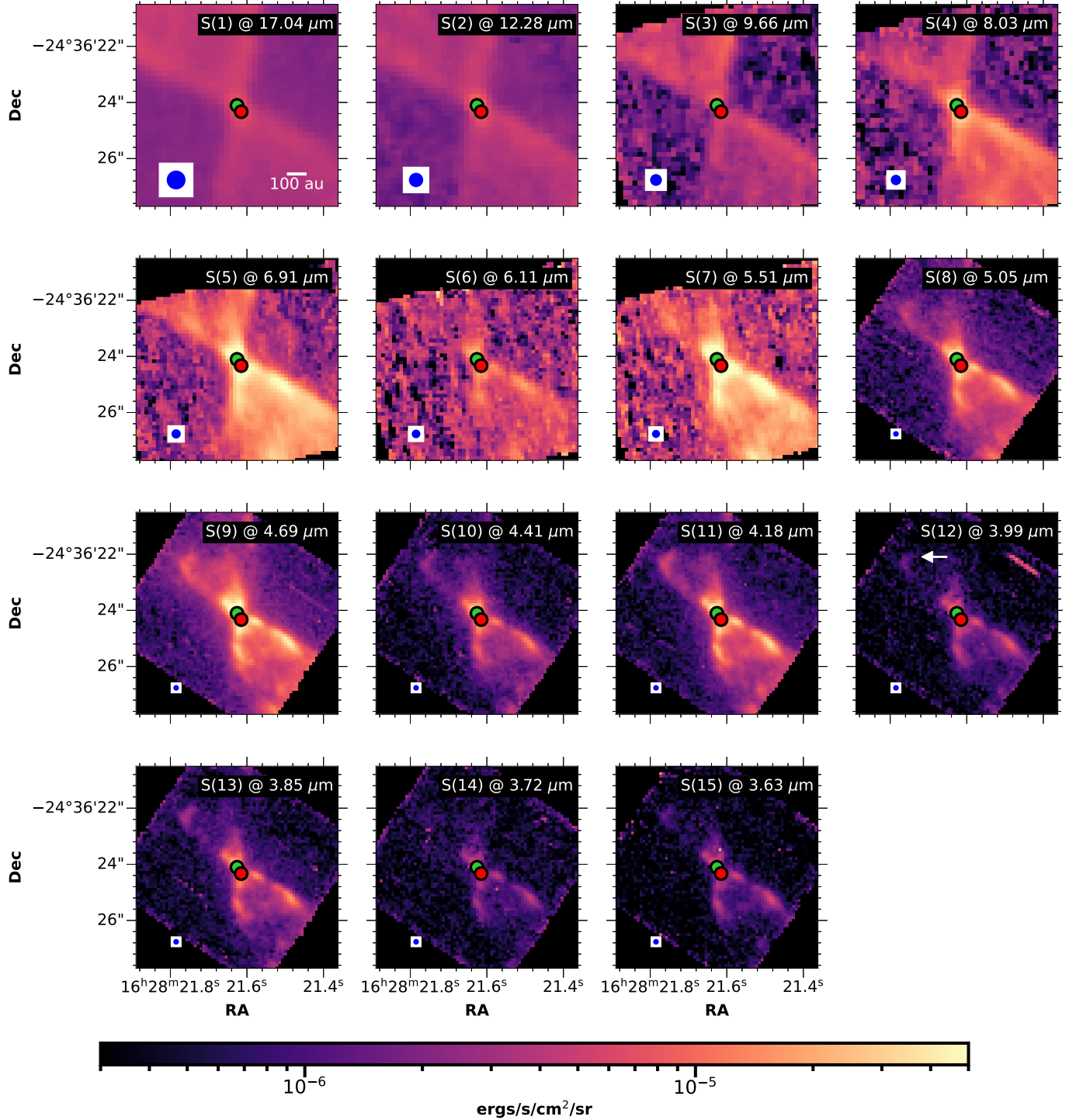


Figure 5. The morphology of the H_2 0-0 S lines from S(1) to S(15). The green marker is the MRS 14 μm position, while the ALMA 1.3 mm position is shown as the red marker. A scale bar corresponding to 100 au is shown in the bottom right corner (of the S(1) image), while the JWST PSF FWHM is shown in the bottom left corner as the blue circle. We also highlight the location of the spur in H_2 as a white arrow in the S(12) image. See Table 2 for wavelength information for the H_2 transitions.

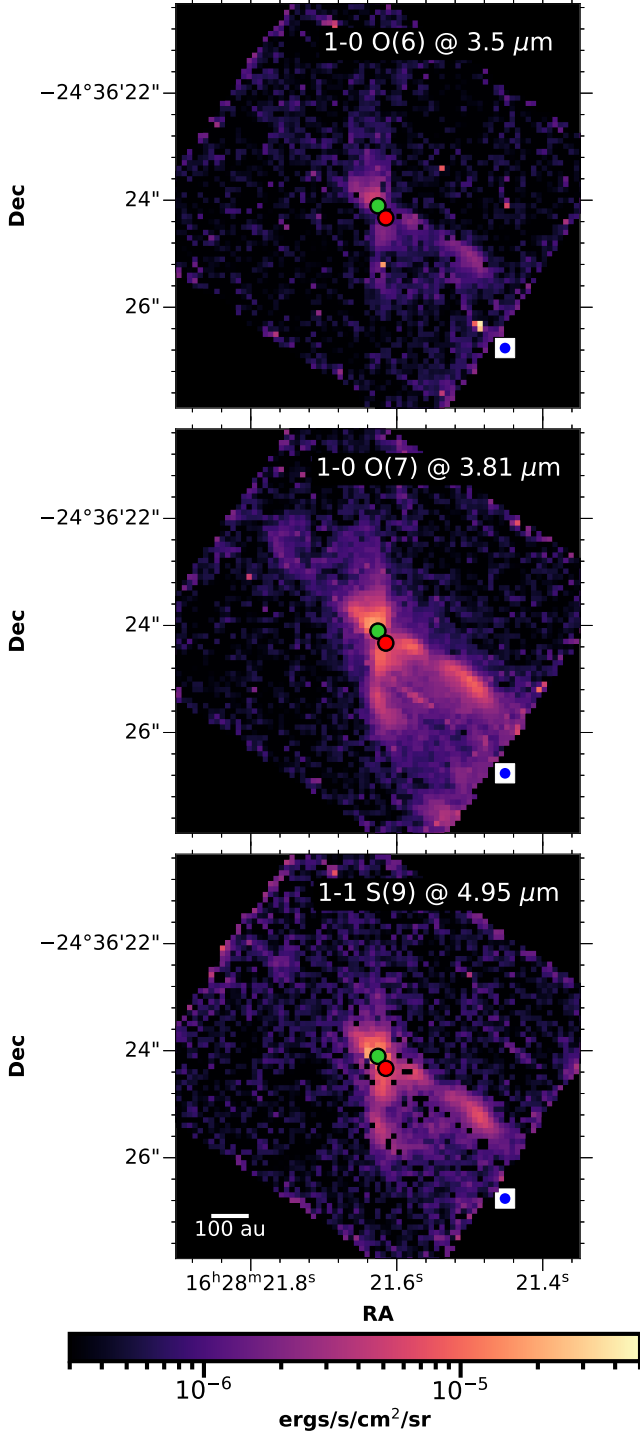


Figure 6. The morphology of the high excitation H_2 lines detected towards IRAS 16253–2429. The green marker is the MRS 14 μm position, while the ALMA 1.3 mm position is shown as the red marker. A scale bar corresponding to 100 au is shown in the bottom left corner, while the JWST PSF FWHM is shown in the bottom right corner as the blue circle.

blue-shifted jet/outflow. The positional offset, however, does not have any major effects on the remainder of this study, but can be an important parameter for improving the radiative transfer model of the protostar.

3.3. H_2 Emission in the Cavity

In Figure 5, we show the maps of the detected H_2 0-0 $S(J)$ lines towards IRAS 16253–2429 ranging from $J = 1$ to $J = 15$ (see Table 2 for spectroscopic details). At every pixel, a local (line-free) continuum was subtracted, then a Gaussian fit to the continuum subtracted line profile was made, and the integrated flux (from the area of the Gaussian) at each pixel was computed. However, the signal-to-noise ratio (S/N) for H_2 0-0 $S(3)$ and H_2 0-0 $S(6)$ is notably lower. This is because the H_2 0-0 $S(3)$ line falls within the 10 μm silicate feature, while the H_2 0-0 $S(6)$ line is situated within the 6 μm H_2O ice feature. All the H_2 0-0 $S(J)$ lines trace the protostellar molecular outflow and exhibit an hourglass-like shape similar to the ^{12}CO outflow detected at (sub)millimeter wavelengths (Hsieh et al. 2016; Yen et al. 2017; Hsieh et al. 2019; Aso et al. 2023). Based on the velocities measured in Section 3.5, we interpret the H_2 as emission from a warm, molecular outflow. Furthermore, we observe weak extended emission for H_2 lines beyond the boundaries of the cavity, as delineated by the NIRSpec continuum. This may be ambient emission from the surrounding molecular cloud (also see Tyagi et al., in prep).

In addition to the H_2 0-0 $S(J)$ lines, extended emission from transitions of H_2 1-0 $O(J)$ and H_2 1-1 $S(J)$ lines are also detected. These are rotational line in the upper $v = 1$ state, that can be used to compute the vibrational temperature. In Figure 6 we show the bright ro-vibration lines detected in NIRSpec IFU. Despite the low S/N of these lines, their morphology is similar to that of the high-excitation ($J \geq 8$) H_2 0-0 $S(J)$ lines. However, no H_2 1-0 $Q(J)$ transitions were detected from the protostar.

The H_2 outflow emission from IRAS 16253–2429 is not symmetric between the northern and southern cavities. We find that for higher- J transitions of H_2 the southern cavity (red-shifted) is much brighter than the northern side (opposite to what we found for the continuum emission). This suggests that the excitation of the H_2 is different between the two lobes; this will be explored in a subsequent paper. The low transition lines fill the cavities with an enhancement towards the wall of the cavity indicating limb brightening due to shocks along the cavity wall. For higher transitions, the flow is narrower in the northern cavity. This cavity also shows a spur (Figure 5) toward the jet (also see Federman et al. 2024). In the southern cavity, bright emission is seen

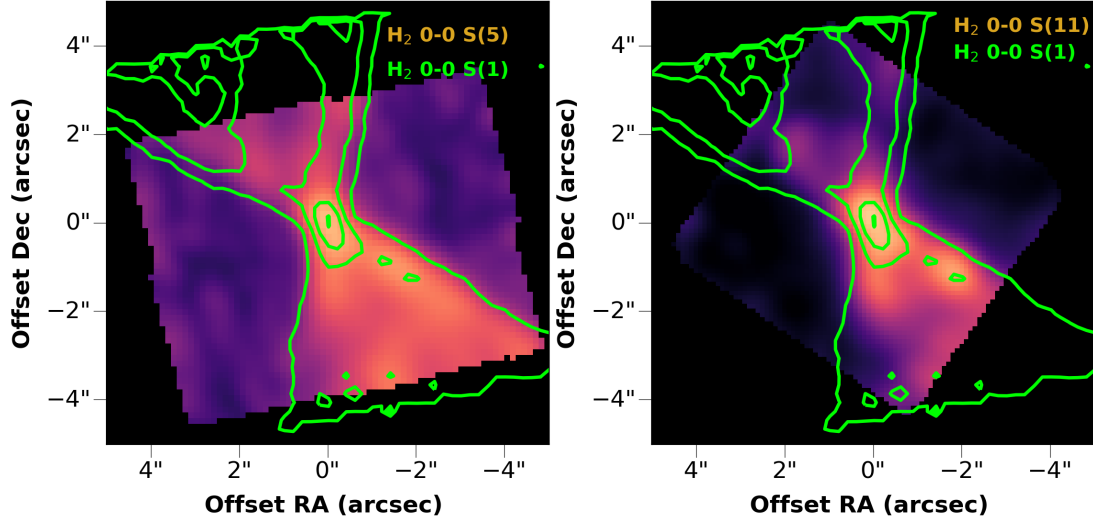


Figure 7. A comparison of the width of the outflow, as traced in H_2 0-0 S(1) (as lime contours) with the width of the outflow traced in H_2 0-0 S(5) and H_2 0-0 S(11) (in color scale). The H_2 0-0 S(5) and H_2 0-0 S(11) images have been convolved to the same resolution as S(1) and each panel is on a common pixel scale. H_2 0-0 S(1) contours are 40%, 60%, 80% 99% \times peak line intensity of $7.8 \times 10^{-6} \text{ erg s}^{-1} \text{ cm}^2 \text{ sr}^{-1}$.

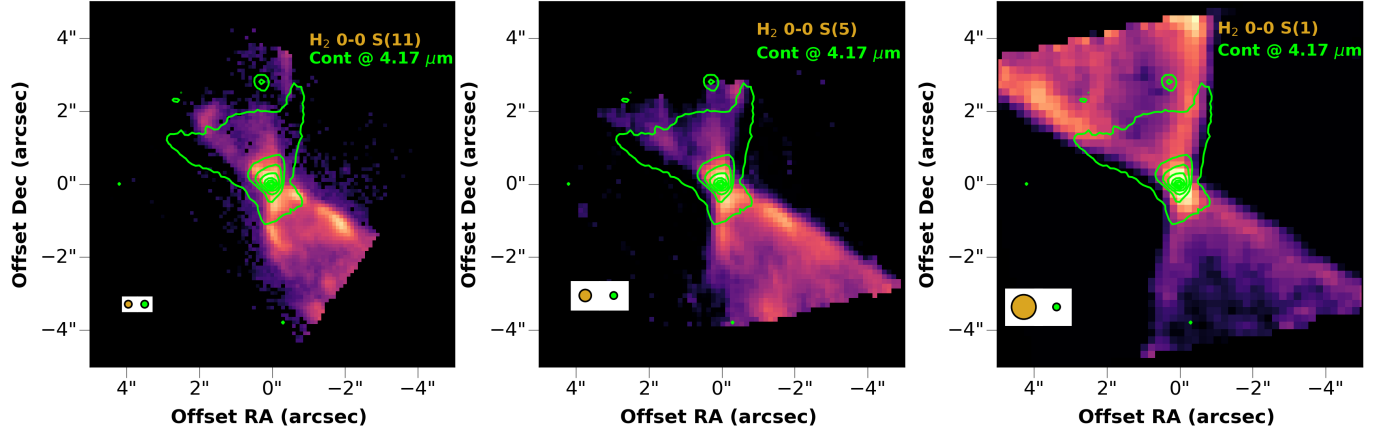


Figure 8. A comparison of the cavity seen in scattered light in the continuum at $4.17 \mu\text{m}$ (lime contours) and the H_2 0-0 S lines from NIRSpec and MIRI wavelength range (color scale). The NIRSpec continuum contours are 1%, 5%, 10%, 20%, 40%, 60%, 80%, 99% \times peak continuum intensity of $2.09 \text{ MJy } \mu\text{m} \text{ sr}^{-1}$. The JWST PSF is shown in the bottom left corner (lime for the NIRSpec continuum and khaki for the H_2 lines)

along the cavity edge. On the northern cavity, only a small length along the NW wall shows emission in the higher transitions.

When comparing the morphology of various transitions of H_2 (Figure 5), it is evident that the higher energy transitions of H_2 appear to be more collimated and delineate a narrower outflow compared to lower energy transitions. However, it is important to note that the various H_2 lines have different resolutions, ranging from $0.^{\prime\prime}2$ to $\sim 0.^{\prime\prime}67$ (Federman et al. 2024; Law et al. 2023). Therefore, to ensure a fair comparison, we convolved the H_2 emission lines to the common spatial resolution of the 0-0 S(1) line. In Figure 7, we superimposed the con-

volved maps of H_2 0-0 S(5) and S(11) (chosen for their high S/N) on top of the H_2 0-0 S(1) line (at $17.035 \mu\text{m}$). The outflow traced in 0-0 S(1) appears to be broader than the outflow observed in S(5) and S(11), even after convolution (to a common spatial resolution); this effect is more pronounced on the northern side.

3.4. H_2 Emission in context of Scattered Light Continuum and the ALMA ^{12}CO Outflow

We next analyzed the width of the H_2 emission and compared it with the width of the scattered light cavity observed using NIRSpec. In Figure 8, we overlay the NIRSpec continuum on the H_2 emission lines. We examined how the morphology of the H_2 lines corre-

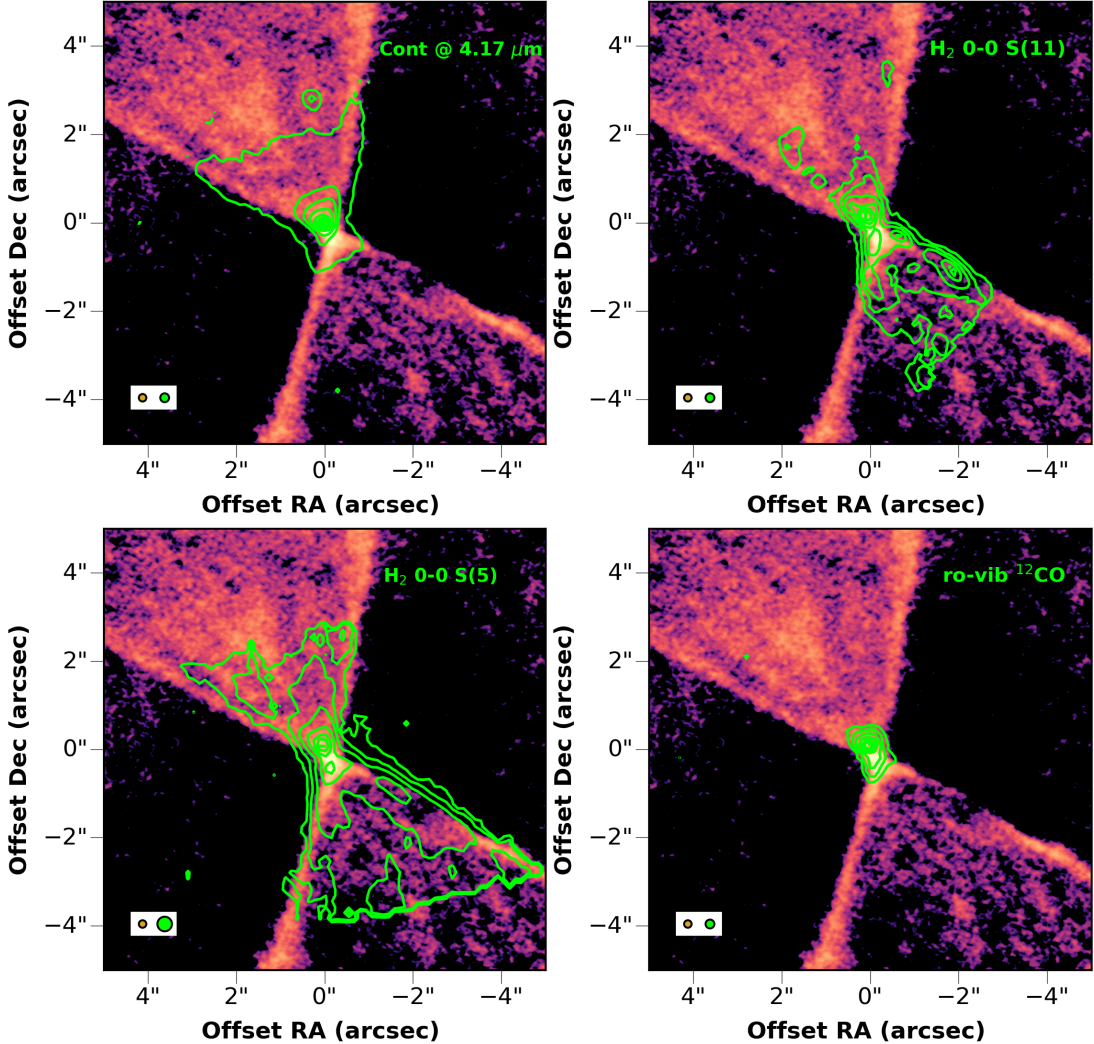


Figure 9. The ALMA integrated intensity CO 2-1 (robust=0.5) emission map (color scale) with the JWST continuum at $4.17 \mu\text{m}$, H_2 0-0 S(11), H_2 0-0 S(5) and the ro-vibrational ^{12}CO lines as lime contours. The contours are 5%, 10%, 20%, 40%, 60%, 80%, 99% \times peak (line) intensity for the gas lines, while the outer-most contour for the continuum is at 1% level. The JWST PSF (lime circle) and the maximum ALMA beam (khaki circle) is shown in the bottom left corner.

sponds to the $4.17 \mu\text{m}$ continuum cavity, focusing on three high-S/N lines: 0-0 S(11), 0-0 S(5) and 0-0 S(1). The 0-0 S(11) line has a resolution of $\sim 0.^{\prime\prime}2$ (Federman et al. 2024), comparable to the resolution of the continuum cavity, while 0-0 S(5) has a slightly lower resolution of $\sim 0.^{\prime\prime}33$ and 0-0 S(1) has a resolution of $\sim 0.^{\prime\prime}67$ (Law et al. 2023). The H_2 emission is narrower than the 1% contour of the scattered light continuum tracing the cavity wall on the northern side, not only for the higher energy transitions but also for S(1).

Aso et al. (2023) recently studied the molecular outflow from IRAS 16253-2429 at high resolution. These observations revealed a wide-angle bipolar outflow detected in ^{12}CO $J = 2-1$ (also see Figure 1b), but no collimated molecular jet was detected. The bulk of the ^{12}CO emission has a velocity within $\pm 4 \text{ km s}^{-1}$ of the systemic

V_{LSR} of the protostar of $\sim 4 \text{ km s}^{-1}$. In Figure 9 we show the ALMA ^{12}CO $J = 2-1$ outflow (integrated from -1 to 10 km s^{-1} , robust = 0.5) superimposed on the NIRSpec continuum, H_2 lines, and the ro-vibrational ^{12}CO lines detected in NIRSpec (Rubinstein et al. 2024). The resolution of the ^{12}CO $J = 2-1$ ($0.^{\prime\prime}17 \times 0.^{\prime\prime}13$) is better than the NIRSpec resolution of $\sim 0.^{\prime\prime}2$ (Federman et al. 2024) and the MIRI resolution ($0.^{\prime\prime}33$) at the wavelength of the H_2 S(5) line.

The scattered light cavity (traced by the NIRSpec continuum) exhibits a width slightly wider than that of the ALMA ^{12}CO $J = 2-1$ outflow across the northern outflow. The 1% contour of the continuum extends slightly beyond the CO emission, which could also be due to a combination of angular resolution and penetration of scattered light beyond the cavity wall. The low-

Table 2. The H₂ lines analyzed in this work. The wavelength, Einstein A coefficient A_{ul} , and upper state energy are from Gordon et al. (2022). The symbol * indicates that the lines are not pure rotational transitions.

Wavelength μm	Name	A_{ul} s ⁻¹	E_{up} K
17.035	H ₂ 0-0 S(1)	4.8×10^{-10}	1015
12.279	H ₂ 0-0 S(2)	2.8×10^{-9}	1682
9.665	H ₂ 0-0 S(3)	9.8×10^{-9}	2504
8.025	H ₂ 0-0 S(4)	2.6×10^{-8}	3475
6.910	H ₂ 0-0 S(5)	5.9×10^{-8}	4586
6.109	H ₂ 0-0 S(6)	1.1×10^{-7}	5830
5.511	H ₂ 0-0 S(7)	2.0×10^{-7}	7197
5.053	H ₂ 0-0 S(8)	3.2×10^{-7}	8677
4.954*	H ₂ 1-1 S(9)	4.3×10^{-7}	15722
4.695	H ₂ 0-0 S(9)	4.9×10^{-7}	10261
4.41	H ₂ 0-0 S(10)	7.0×10^{-7}	11940
4.181	H ₂ 0-0 S(11)	9.6×10^{-7}	13703
3.996	H ₂ 0-0 S(12)	1.3×10^{-6}	15540
3.846	H ₂ 0-0 S(13)	1.6×10^{-6}	17444
3.807*	H ₂ 1-0 O(7)	1.1×10^{-7}	8365
3.724	H ₂ 0-0 S(14)	2.0×10^{-6}	19403
3.626	H ₂ 0-0 S(15)	2.4×10^{-6}	21411
3.501*	H ₂ 1-0 O(6)	1.5×10^{-7}	7584

J H₂ (with $E_{up} \leq 5000$ K) emission also has a similar width to the ALMA ¹²CO $J = 2-1$ outflow in the northern and southern cavities. The high- J (with $E_{up} > 5000$ K) H₂ emission is narrower in the northern part of the outflow but extends across the entire southern ALMA ¹²CO (2-1) outflow, extending to the cavity walls. The ro-vibrational ¹²CO emission is concentrated at the central protostar and appears to trace the neck of the cold molecular ¹²CO $J = 2-1$ from the outflow.

3.5. Velocity Structure of the H₂ flow

To investigate the velocity structure within the H₂ outflow, we generated velocity maps of the H₂ 0-0 S(4) and H₂ 0-0 S(5) lines at 8.02 μm and 6.91 μm, respectively. These lines have high S/N as well as high spectral and spatial resolution (as well as being a close pair of ortho and para H₂ lines). The velocity maps serve as a valuable diagnostic tool for discerning the kinematic structure within the jets and outflows. During the Gaussian fitting procedure used to generate line maps, one of the extracted parameters is the line center. By mea-

suring shifts in the line center, we can derive velocity shifts, which in turn are used to construct velocity maps. To make the velocity maps we have masked pixels with emission $< 6 \sigma$. We further correct for any systematic offset in the velocity by computing the mean velocity of the velocity maps and subtract that out from each pixel.

In Figure 10, we show the velocity maps of the H₂ 0-0 S(4) and H₂ 0-0 S(5) lines. We find that the maximum (blue-shifted or red-shifted) velocity of the outflow (as observed) is ~ 20 km s⁻¹ (after correcting for systemic velocity) and if we correct for inclination (with inclination angle of 64°) the maximum velocity is ~ 45 km s⁻¹. We find that similar to the ¹²CO $J = 2-1$ line seen in ALMA, the northern outflow is blue-shifted, and the southern outflow is red-shifted. This shows that the H₂ emission is tracing a bipolar outflow in the central cavity surrounding the central jet. The H₂ flow from the protostar is however much faster than the ¹²CO $J = 2-1$ (see Figure 1b and Aso et al. 2023), which has a radial velocity of 1.5-2.5 km s⁻¹ and after correcting for inclination has a radial velocity of 3.4 to 5.7 km s⁻¹. The H₂ velocity in turn is much slower than the jet velocity of 169 ± 15 km s⁻¹ (Narang et al. 2024). We further note that at the protostellar location part of the blue (or red) shifted emission bleeds into the red (or blue) shifted emission for both the H₂ and ¹²CO ALMA emission. This could be due to disk rotation (see Tyagi et al. in prep).

Next, we constructed position velocity (PV) diagrams for the H₂ 0-0 S(1) to S(7) lines that were detected in MIRI MRS after subtracting the cloud velocity. As stated before, we found that there is an extended component to the H₂ emission (see Figure 5). This component might be tracing the ambient emission from the cloud. This cloud component has a smaller velocity than the outflow component from the protostar. We used two 0.8'' radius apertures on either side of the outflow (with offsets of $\delta_1\text{RA} = -2.8''$; $\delta_1\text{Dec} = 0.8$ and $\delta_2\text{RA} = 2.8''$; $\delta_2\text{Dec} = -0.8$, with respect to 14 μm position) to compute the velocity of this weak, slow cloud component. We fit a gaussian to this emission and derive the cloud emission, which we subtract from the data-cube pixel-by-pixel to remove the cloud component and derive the true velocity. After subtracting this ambient component, we extracted velocities from a rectangular region that was 5'' long and 4'' wide and aligned along the outflow direction (PA = 23°) and centered at the 14 μm position. To remove any velocity offsets arising from instrumental or systematic effects, we subtract the mean velocity of the PV diagram, which we define as the mean flow velocity. All velocities measured from the PV diagram are therefore expressed relative to this mean flow

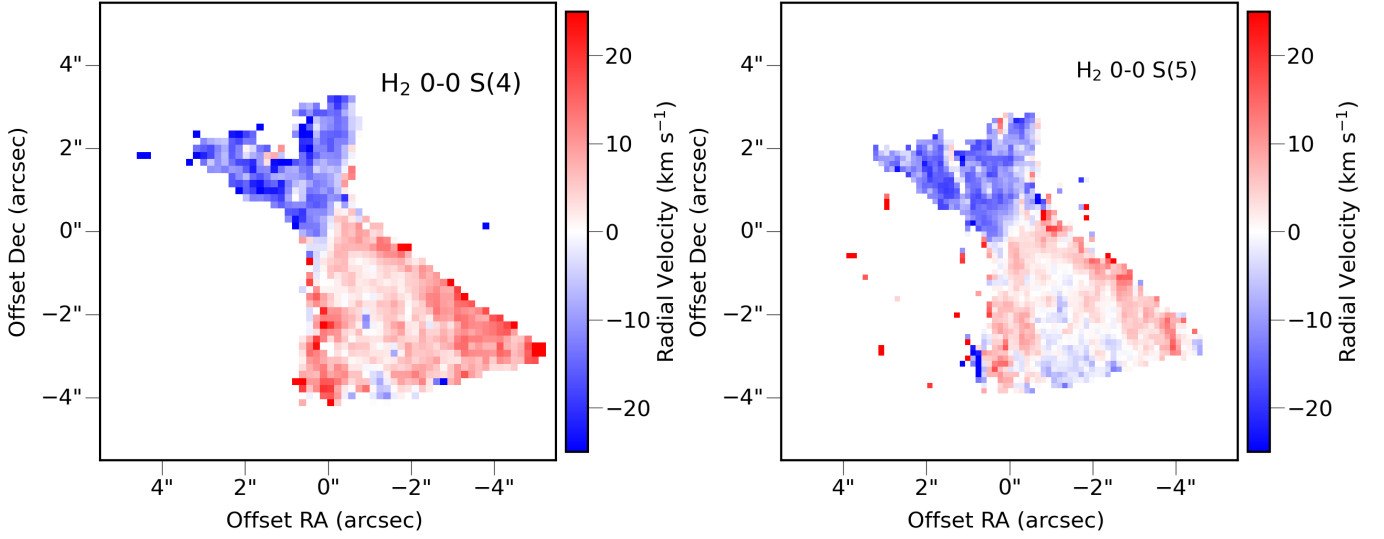


Figure 10. Velocity maps of the H_2 0-0 S(4) and H_2 0-0 S(5) lines at $8.02 \mu\text{m}$ and $6.91 \mu\text{m}$.

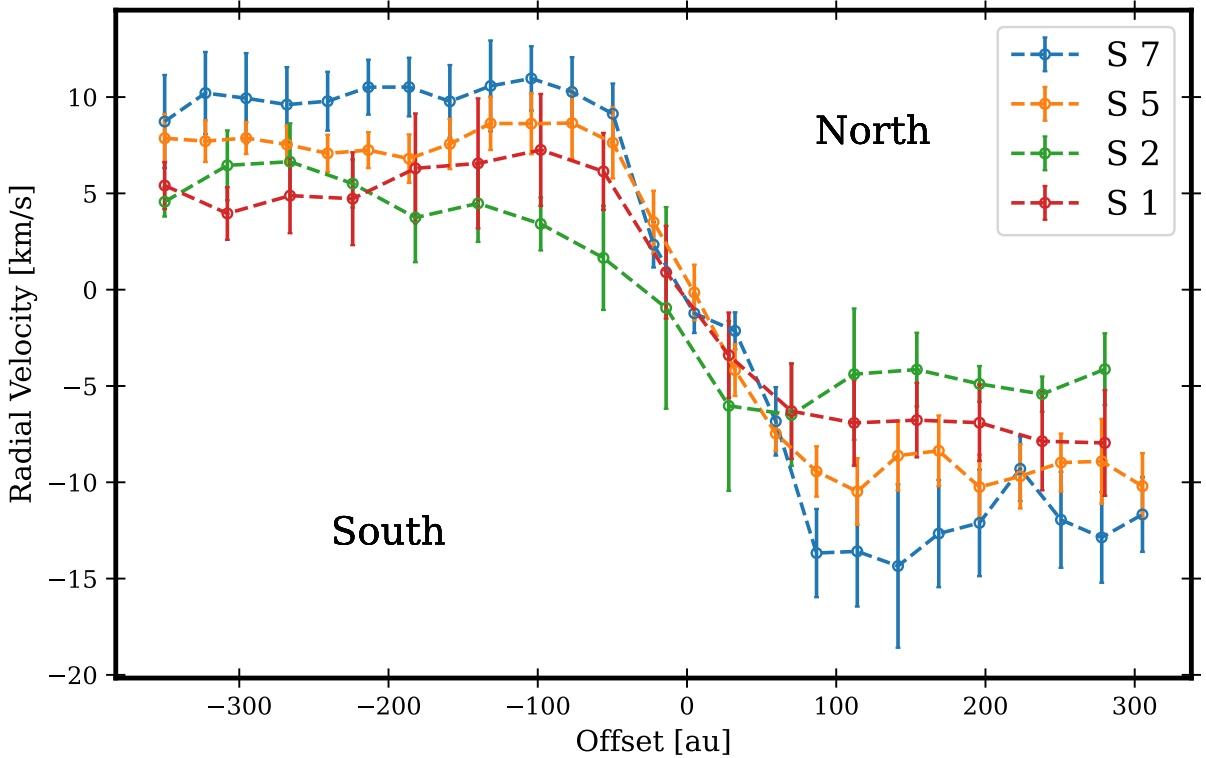


Figure 11. Position velocity (PV) diagram for the H_2 0-0 S(1), S(2), S(5) and S(7) lines extracted along the outflow direction. The error bars on the line are the errors in determining the velocity center of the line in each bin. We have set the mean flow velocity to zero due to uncertainties in the absolute velocity calibration.

velocity. In Figure 11, the PV diagrams for the various molecular H_2 0-0 S(J) lines are shown.

The low excitation H_2 0-0 S(1) and H_2 0-0 S(2) lines have radial velocities in the range of $\sim \pm 5.5 \text{ km s}^{-1}$, while the higher transitions such as H_2 0-0 S(5) and H_2 0-0 S(7) have a radial velocity range between ~ -10 to 7 km s^{-1} and ~ -15 to 10 km s^{-1} respectively. This suggests that the higher excitation H_2 (hotter component of the outflow) is moving faster than the cooler low excitation gas component of the outflow as traced in low- J H_2 . If we further correct for inclination (with inclination angle of 64°), we find that the low- J H_2 outflow (S(1) and S(2)) has a velocity of $\sim 12.5 \text{ km s}^{-1}$, while the hotter component as traced by H_2 0-0 S(5) and S(7) has a velocity of 28.5 km s^{-1} . There could be an even faster component of the H_2 outflow but due to the poorer velocity resolution of NIRSpec we are not able to detect it.

3.6. Opening angle of the outflow

From Figure 7 and Figure 9, it is evident that the different tracers of the outflow (with different excitation energy) have different spatial extents. However, to quantify this the difference in opening angle and the width of the outflow as a function of distance from the driving source need to be measured. To do so we first need to delineate the outer edge of the emission. We adopted a method similar to that of Habel et al. (2021), where we initially rotated the image by 23° clockwise to align the outflow axis with the positive (y)-axis in an x - y Cartesian plane. The rotation angle, 23° , was calculated from (PA of the disk) - 90° , and the PA of the disk, 113° , was determined by modeling the disk and is measured from the east of north (Aso et al. 2023 and Narang et al. in prep). We computed a second-order differential along the x-axis, and the inflection points (where the second-order derivative equals zero) delineate the edge of the cavity. Using this approach, we obtained four cavity edges (two for each of the blue- and red-shifted outflows/cavities). A similar method was also used by Pascucci et al. (2025) to measure the opening angle of the outflow for four edge-on sources. To avoid bad pixels and low S/N data we only used pixels with $S/N > 7\sigma$.

In Figure 12, we present the cavity edge as traced by this method. Our analysis reveals that the cavity edges deviate from a straight line and exhibit structural features. One prominent feature observed in the molecular H_2 0-0 S(5) and S(11) emission is a notch in the outflow, located at $\sim -4''$ offset along the height of the outflow to the south. This same notch region corresponds to an emission minimum in both H_2 0-0 S(1) and ALMA ^{12}CO . In addition, H_2 0-0 S(5) and S(1) show an out-

Table 3. The (deconvolved) opening angle, measured as the half-width of the outflow as a function of distance from the central protostar, derived for the high-S/N H_2 lines and the ALMA ^{12}CO outflow.

Line	Opening Angle (°)	
	Northern Outflow	Southern Outflow
^{12}CO J=2-1	38 ± 0.3	40 ± 0.3
S(1)	41 ± 1	40 ± 1
S(2)	38 ± 1	35 ± 1
S(3)	39 ± 1	33 ± 1
S(4)	39 ± 2	36 ± 2
S(5)	36 ± 1	34 ± 1
S(7)	25 ± 4	29 ± 1
S(11)	21 ± 3	19 ± 2

flow neck within $\sim 1''$ on both sides of the protostellar position, where the edge is almost parallel to the y-axis, and a similar neck is also seen in ^{12}CO within $\sim 0.5''$ on both sides.

To measure the opening angle of the outflow, we determined the half-width of the cavity as a function of distance from the central protostar (indicated as offset along the height in Figure 12) by fitting a straight line. The inner $1''$ on both sides of the protostellar position was masked to exclude the outflow neck. We further deconvolve the measurements by subtracting, in quadrature, the maximum beam/PSF radius from both the half-width of the cavity and the offset measured along the cavity height. In Table 3 we have listed the (deconvolved) opening angle for the flow traced by H_2 0-0 rotational lines with high S/N along with the ALMA ^{12}CO . We find a gradual decrease in the opening angle of the outflow with an increase in E_{up} . Specifically, the opening angle decreases from $40\text{--}35^\circ$ for the low- J H_2 lines (up to S(5)) and the cold gas component (ALMA ^{12}CO) to $\sim 28\text{--}19^\circ$ for the high- J H_2 lines (S(7)–S(11)).

3.7. Width of the Outflow at the the Protostar

Figure 13 presents the ALMA 1.3 mm continuum contours superimposed on the JWST continuum map at $4.17 \mu\text{m}$, alongside the line maps for H_2 0-0 S(5), H_2 0-0 S(11), and [Fe II] at $5.34 \mu\text{m}$ lines. We observe that the disk traced by the 1.3 mm dust continuum is not only narrower than the scattered light cavity, but also smaller than the H_2 outflow and the jet traced by [Fe II] at $5.34 \mu\text{m}$. Given that the ALMA observations of the continuum disk have a much higher resolution

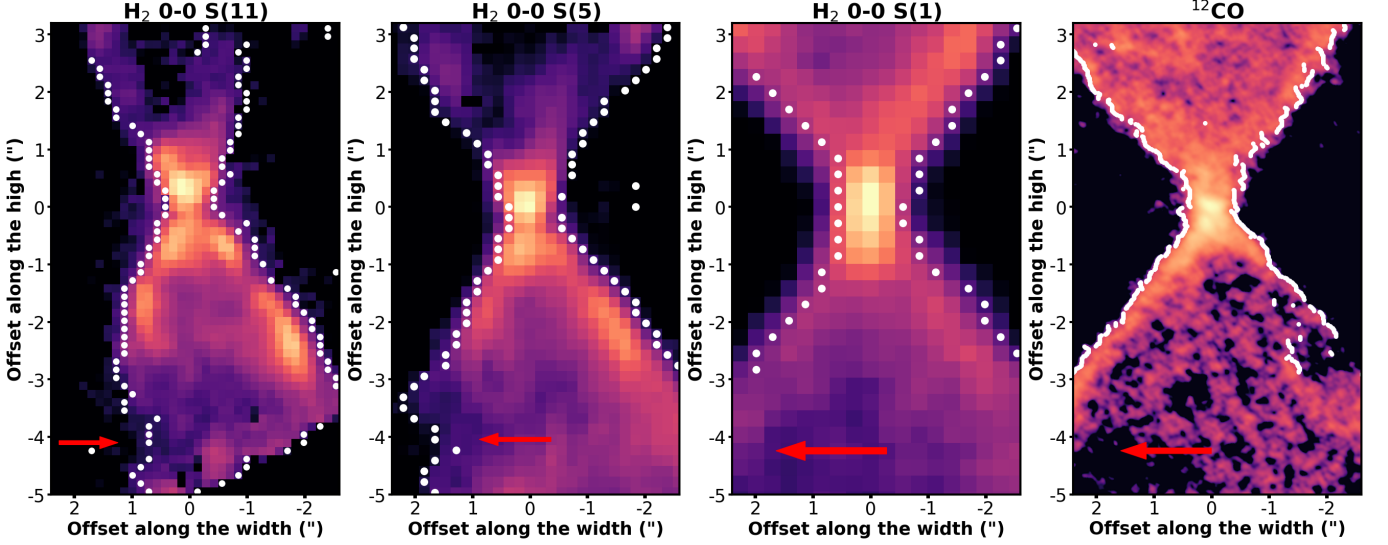


Figure 12. An illustration of the detected edges of the molecular outflow. The color scale is the outflow and the edge is shown as white points. All images are cropped to the same area. We show a red arrow that illustrates the position of the notch in the outflow.

($0.^{\prime\prime}073 \times 0.^{\prime\prime}048$) than the JWST observations, deconvolution of the MIRI and NIRSpec images is necessary to accurately measure the true width of the outflow at its base.

To quantify the width of the H_2 outflow at the base of the protostar ($14 \mu\text{m}$ position) and compare it with the protostellar disk (both dust and gas), we adopt a method similar to Narang et al. (2024). We took slices perpendicular to the jet/outflow axis with a width of 2 pixels (NIRSpec beam is $0.^{\prime\prime}2$ or 2 pixels). Subsequently, each slice was fitted with a Gaussian, and the Full Width at Half Maximum (FWHM) of the Gaussian was measured as the width of the outflow in that slice. To measure the width of the outflow, we used the H_2 0-0 S(11) line due to its high S/N and spatial resolution.

In Figure 14(a), we show the H_2 0-0 S(11) emission map with the slices marked in green. We measure the width of the slice closest to the protostar and show it in Figure 14(b). The width of the outflow from the fit is $\sim 0.32 \pm 0.01$ ". This is larger than the PSF of NIRSpec IFU at $0.2''$. We deconvolve the outflow width using the NIRSpec IFU average PSF and obtain a deconvolved outflow width of $\sim 0.25''$. At the distance of IRAS 16253–2429 this translates into 35 au. However, this width should be regarded as an upper limit for several reasons. First, the measurement is averaged over two pixels, which inherently broadens the observed profile, even though we have subtracted out the PSF. Second, the outflow cross-section does not follow an exact Gaussian shape, so fitting it as a Gaussian can overestimate its true width. Together, these factors reinforce

that the derived width represents a conservative upper bound rather than a precise physical measurement.

The H_2 outflow width is much larger than the width of the [Fe II] emission (at $5.34 \mu\text{m}$) of $20–23$ au (Federman et al. 2024; Narang et al. 2024). The ALMA 1.3 mm continuum dust disk and the Keplerian gas disk (traced by ^{12}CO) associated with IRAS 16253–2429 are about 30 au wide (Aso et al. 2023) which is slightly smaller than but comparable to the width of the outflow as traced by H_2 .

4. ORIGIN OF THE OUTFLOW FROM IRAS 16253–2429

Our observations of IRAS 16253–2429 using JWST and ALMA reveal a nested outflow morphology. The hourglass shape first detected by Spitzer IRAC is traced in gas by the bipolar wide-angle outflows seen in H_2 and ^{12}CO in the inner ~ 2000 au of the protostar. The outflow cavity walls are best traced by the NIRSpec continuum and the cold ^{12}CO emission from ALMA. Near the base of the protostar, the width of the molecular H_2 emission, as traced by the 0-0 S(11) line, is slightly smaller than the diameter of the continuum disk and the diameter of the Keplerian gas disk (traced in ^{12}CO) around the protostar.

When examining the flow traced by various H_2 transitions, we find that the higher- J transitions (of S(7) and S(11) with $E_{up} > 5000$ K) trace a much narrower outflow (based on the opening angle) as compared to the low- J H_2 transitions ($E_{up} \leq 5000$ K) and ALMA ^{12}CO $J = 2-1$ ($E_{up} \sim 30$ K) (see Table 3). As the E_{up} of the molecular tracer in the outflow increases, the outflow's opening angle narrows from $\sim 40\text{--}35^\circ$ for ^{12}CO and low-

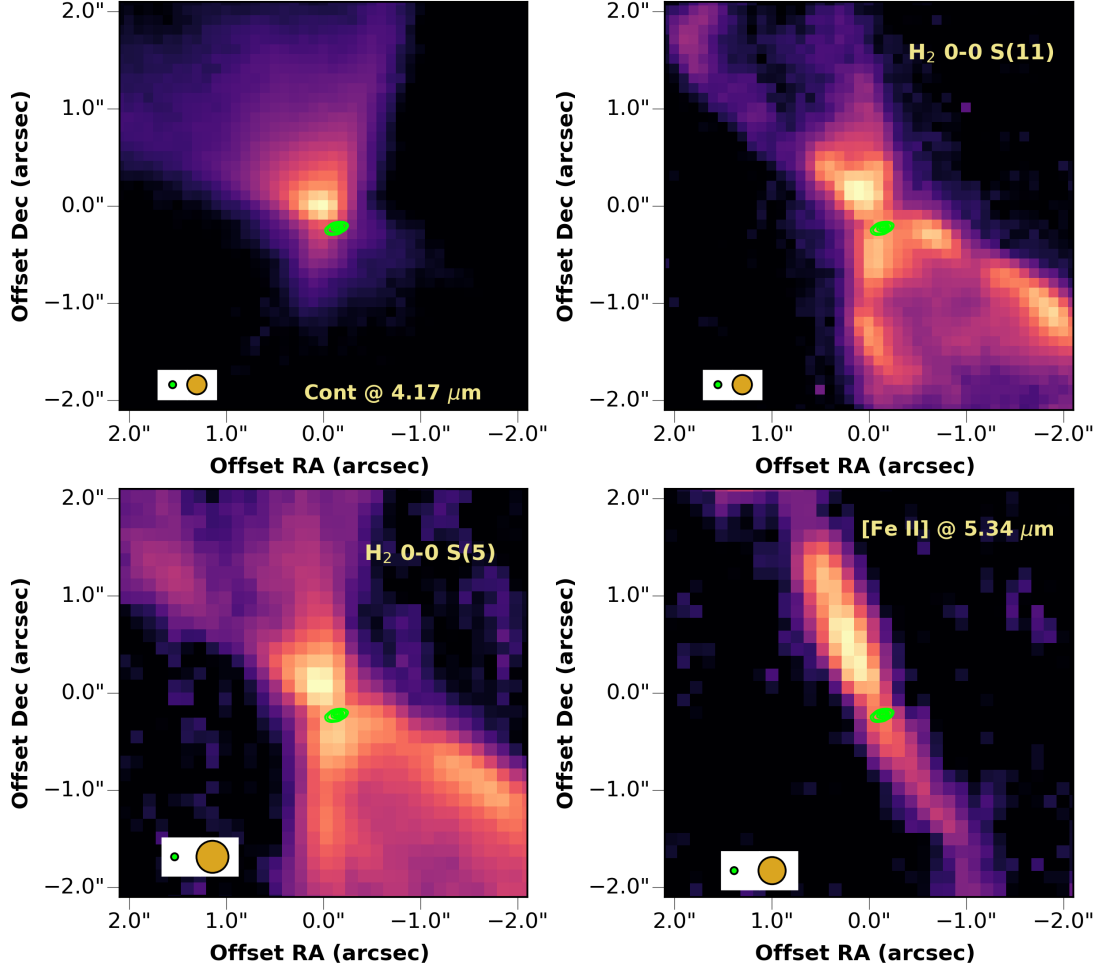


Figure 13. The ALMA 1.3 mm continuum (lime contours) overlaid on top of the JWST continuum at $4.17 \mu\text{m}$, H_2 0-0 S(11), H_2 0-0 S(5) and the $[\text{Fe II}]$ line at $5.34 \mu\text{m}$ in color scale. The 1.3 mm contours are 10%, 20%, 40%, 60%, 80% 99% $\times 5.1 \text{ mJy/beam}$. The JWST PSF as khaki circle and the maximum ALMA continuum beam (of $0.073''$) as lime circle are shown in the bottom left corner.

J H_2 to $28\text{-}19^\circ$ for high- J H_2 . This molecular outflow surrounds a highly collimated (opening angle of $2.6^\circ \pm 0.5^\circ$) atomic/ionic jet detected in multiple $[\text{Fe II}]$ transitions, as well as $[\text{Ne II}]$, $[\text{Ni II}]$, $[\text{Ar II}]$ and H-I ($\text{Br}\alpha$) with JWST (Narang et al. 2024; Federman et al. 2024).

Similar outflow and jet morphology have been observed in the Class I protostar TMC 1E (Tychoniec et al. 2024), where the fine-structure jet is highly collimated and is surrounded by a much wider molecular outflow. Tychoniec et al. (2024) found that the degree of collimation increases with increasing E_{up} for the molecular H_2 and that the molecular H_2 outflow was more collimated than the ALMA ^{12}CO outflow and scattered light cavity, similar to what we find for IRAS 16253-2429. Such a nested morphology was also detected in DG Tau B (also a Class I protostar) (Delabrouse et al. 2024) using a combination of ALMA, JWST, and ground-based VLT observations with SINFONI.

Recently, Pascucci et al. (2025) reported similar results for the edge-on source HH30, finding a highly collimated jet surrounded by molecular H_2 and a cold ^{12}CO outflow. They observed that the H_2 emission was more collimated than the ^{12}CO outflow detected with ALMA. Based on the combination of this nested morphology and a small launch radius ($\sim 7 \text{ au}$), Pascucci et al. (2025) argued that radially extended magnetohydrodynamic (MHD) disk winds were the only mechanism consistent with the nested jet and outflow structures observed in their sample.

In contrast to the more evolved protostars and Class II disks in the previous studies, IRAS 16253-2429 is in the envelope dominated, Class 0 stage, where most of the mass accretion occurs (Fischer et al. 2017). It is in this phase where the interaction of disk launched winds and jets with the infalling envelope entrains gas and regulates the masses of stars (Hsieh et al. 2023). This interaction must occur along the cavity walls. Our data

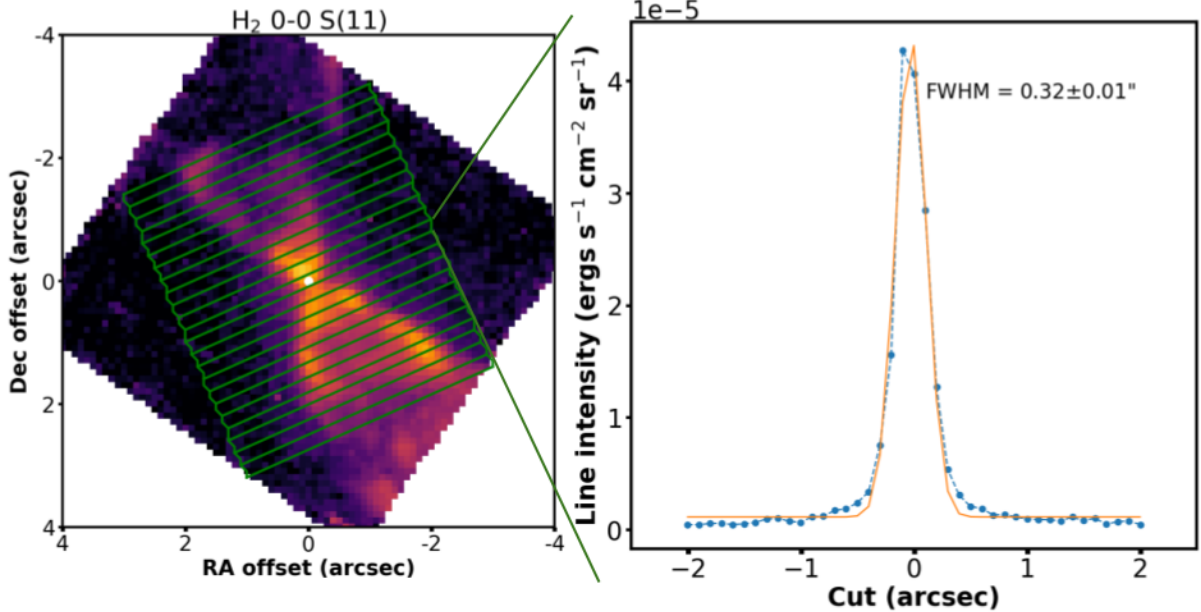


Figure 14. (a) The slices aligned with the jet and overlaid in green on top of the molecular outflow traced in H_2 S(11) at $4.18 \mu\text{m}$ within which the width of the outflow is measured. The white circle represents the $14 \mu\text{m}$ protostellar position. (b) The Gaussian fit to the intensity profile for the slice at the protostellar position.

on the Class 0 protostar IRAS 16253-2429 clearly show a wide angle wind traced by the H_2 is directly interacting with the envelope along the cavity walls. We see the H_2 emission extend through the cavities. Along the cavity walls, we see enhanced H_2 emission in the lower rotational lines. In addition, in certain areas where the shocks may be less oblique, along a notch in the northern cavity and a curved portion of the southern cavity, we see shocks along the cavity walls in higher transitions. The less oblique shocks in these regions appear to result in warmer shocked gas. Given the lower velocity of the ALMA CO emission (Aso et al. 2023), this component likely traces entrained gas accelerated along the cavity walls, although further analysis is required to rule out a contribution from warm gas in a disk wind.

The MHD disk wind naturally explains the presence of a primarily molecular component of the flow (Panoglou et al. 2012). Evidence for disk winds being the driving mechanism behind the nested structure of IRAS 16253-2429 comes from the analysis of the kinematics of the molecular outflow as traced in H_2 . The position-velocity diagrams reveal a clear distinction in the kinematics of the low- and high-excitation H_2 transitions. The low- J H_2 transitions exhibit relatively low velocities, $\sim 12.5 \text{ km s}^{-1}$ with respect to the mean flow velocity. In contrast, the higher- J transitions, such as H_2 0-0 S(5) and S(7), display significantly higher velocities, around 28.5 km s^{-1} with respect to the mean flow velocity. This

suggests that the higher-energy H_2 emission, not only appears more collimated but is also moving considerably faster compared to the wider, slower-moving low- J H_2 emission. This is consistent with the results of MHD wind simulations, which predicts faster speeds for more collimated parts of the flow (e.g., Pudritz & Norman 1983, 1986; Wardle & Koenigl 1993; Konigl & Pudritz 2000; Pudritz et al. 2007; Pascucci et al. 2023).

In contrast, X-wind models predict that both the jet and the wide-angle wind components are launched from the innermost regions of the disk and therefore should exhibit similar velocities. Within the X-wind framework (Najita & Shu 1994; Shang et al. 2007), the slower H_2 emission we observe would be tracing shocked material within the wind. To reproduce the observed flow, X-wind models must account for both the molecular nature of the warm, slower component and the atomic or ionic composition of the fast, collimated jet, which some recent simulations have begun to achieve (e.g., Shang et al. 2020, 2023a) by introducing the interaction of X-winds with the ambient material.

Recently, Nakatani et al. (2025) demonstrated that photoevaporative winds can exhibit morphological characteristics similar to those of MHD winds, with higher- J H_2 transitions displaying a more collimated structure. However, MHD disk-wind models predict predominantly molecular outflows (e.g., Panoglou et al. 2012), whereas the strong high-energy radiation required to

drive photoevaporative winds can efficiently dissociate H₂, resulting in very low molecular fractions (Wang & Goodman 2017). IRAS 16253-2429 is currently in a quiescent phase and is therefore unlikely to possess a sufficiently strong UV field to drive photoevaporation. Moreover, the models of Nakatani et al. (2025) predict that photoevaporative winds typically reach velocities of $\lesssim 10$ km, s⁻¹, whereas for IRAS 16253-2429 we measure significantly higher velocities, up to ~ 20 km, s⁻¹, albeit with large uncertainties. Finally, the presence of highly collimated atomic/ionic jets traced by e.g., [Fe II], [Ne II], and [Ar II] (Narang et al. 2024) further supports an MHD wind scenario over a photoevaporative origin.

Furthermore, some of the substructures observed in the higher transitions of H₂ such as the one associated with the jet knot (see Figure 5) can be interpreted as a bow-shock and wake driven by internal shocks in the jet (Narang et al. 2024; Federman et al. 2024). These structures can be generated when shocks in jets with fluctuating velocities result in material ejected laterally from the jet (Tabone et al. 2018; Rabenahary et al. 2022). These require a slow moving wind surrounding the jet (Tabone et al. 2018), and they can accelerate the material in the wind (Lee et al. 2021). Thus, the high velocity, more collimated component may be further accelerated by interactions with the jet (Delabrosse et al. 2024; Rabenahary et al. 2022). We further speculate that the shear in the wind flow, both from the interaction with the jet and due to the range of launching speeds in the nested structure, may be responsible for heating of the gas by shocks.

5. SUMMARY

We report the results from joint JWST and ALMA observations of the Class 0 protostar IRAS 16253-2429 in the Ophiuchus molecular cloud (140 pc) that was observed as part of the ALMA large program “Early Planet Formation in Embedded Disks (eDisk)” and the JWST Cycle 1 GO project “Investigating Protostellar Accretion (IPA)”. The key findings from our study are summarized as follows:

1. The continuum cavity traced in the scattered light exhibits a wide hourglass-like morphology, with the northern side appearing brighter and extending further compared to the southern side due to extinction and inclination effects. This cavity follows the shape of the entrained outflow detected with ALMA except at the neck of the hourglass, where the scattered light is wider. At longer wavelengths where scattering is less efficient, the IR emission peak is concentrated toward the central

source, but with a small offset between the emission peak and the ALMA disk position.

2. Within the cavity we detect 15 lines of pure rotational molecular H₂ (v=0-0) emission ranging from S(1) to S(15), along with a few H₂ 1-0 O(J) and H₂ 1-1 S(J) transitions. This emission fills the cavity in the lower transitions, indicating that the cavity is filled with warm, molecular gas.
3. The position velocity diagrams show that low E_{up} H₂ lines (0-0 S(1) and S(2)) have an inclination corrected velocity of ~ 12.5 km s⁻¹ while higher E_{up} lines such as H₂ 0-0 S(5) and S(7) have an inclination corrected velocity of ~ 28.5 km s⁻¹. This velocity structure shows the warm molecular gas filling the cavity is tracing a moderate velocity outflow, slower than the central jet seen in atomic / ionic species.
4. A clear trend is observed in which the outflow opening angle decreases with increasing E_{up}. The angle reduces from 40–35° for the low-J H₂ transitions (up to S(5)) and the cold gas traced by ALMA ¹²CO, to ~ 28 –19° for the higher-excitation H₂ lines (S(7)–S(11)).
5. The outflow (detected in H₂ 0-0 S(11)) is ≤ 35 au wide at the protostellar location. This is slightly larger than but comparable to the diameter of the dust disk (30 au) at 1.3 mm as detected with ALMA as well as the Keplerian disk diameter of ~ 32 au. The width of the outflow however is much wider than the jet width of 20–23 au (as seen in the [Fe II] lines).
6. The observed nested morphology and the kinematics of the jet (as traced in [Fe II] and atomic/ionic lines) and the extended molecular outflow traced in H₂ suggest MHD disk-winds as a possible launching mechanism. The faster, narrower emission in the higher excitation lines appears to be tracing a wake generated by internal shocks within the jet. Thus some of the acceleration of the inner wind may be due to processes in the jet.
7. The ¹²CO observed by ALMA is slower and colder than the molecular wind traced in the warm H₂ gas. This gas may be, at least in part, the entrained gas along the cavity walls accelerated by the molecular wind. Enhancements in low lying H₂ along the cavity edges likely trace oblique shocks tracing the interaction of the wind and entrained gas. In two regions, along the curved wall in the

southern cavity and a notch in the northern cavity, the detection of S(11) emission suggests the presence of hotter, more direct shocks.

This study underscores the synergy between JWST and ALMA in investigating jets and outflows from protostars, demonstrating how these observations can help constrain the mechanisms behind these phenomena.

6. DATA AVAILABILITY

All of the JWST data presented in this article were obtained from the Mikulski Archive for Space Telescopes (MAST) at the Space Telescope Science Institute. The specific observations analyzed can be accessed via DOI: [10.17909/3kky-t040](https://doi.org/10.17909/3kky-t040). The ALMA observations were obtained as part of the ALMA large program Early Planet Formation in Embedded Disks eDisk (2019.1.00261.L, 2019.A.00034.S).

7. ACKNOWLEDGMENT

This work is based on observations made with the NASA/ESA/CSA James Webb Space Telescope. The data were obtained from the Mikulski Archive for Space Telescopes at the Space Telescope Science Institute, which is operated by the Association of Universities for Research in Astronomy, Inc., under NASA contract NAS 5-03127 for JWST. These observations are associated with program #1802. This paper makes use of the following ALMA data: ADS/JAO.ALMA#2019.1.00261.L. ALMA is a partnership of ESO (representing its member states), NSF (USA), and NINS (Japan), together with NRC (Canada), MOST and ASIAA (Taiwan), and KASI (Republic of Korea), in cooperation with the Republic of Chile. The Joint ALMA Observatory is operated by ESO, AUI/NRAO, and NAOJ. The National Radio Astronomy Observatory is a facility of the National Science Foundation operated under cooperative agreement by Associated Universities, Inc. N.O. and M.N. acknowledge support from National Science and Technology Council (NSTC) in Taiwan (NSTC 113-2112-M-001-037) and Academia Sinica

Investigator Project Grant (AS-IV-114-M02). Part of this research was carried out at the Jet Propulsion Laboratory, California Institute of Technology, under a contract with the National Aeronautics and Space Administration (80NM0018D0004). H.T. and P.M. acknowledge the support of the Department of Atomic Energy, Government of India, under Project Identification No. RTI 4002. Support for SF, AER, STM, RG, JG, JJT, and DW in program #1802 was provided by NASA through a grant from the Space Telescope Science Institute, which is operated by the Association of Universities for Research in Astronomy, Inc., under NASA contract NAS 5-03127. LWL acknowledges support from NSF AST-2108794. G.A. and M.O. acknowledge financial support from grants PID2020-114461GB-I00, PID2023-146295NB-I00, and CEX2021-001131-S, funded by MCIN/AEI/10.13039/501100011033. A.C.G. acknowledges support from: PRIN-MUR 2022 20228JPA3A “The path to star and planet formation in the JWST era (PATH)” funded by NextGeneration EU, INAF-GoG 2022 “NIR-dark Accretion Outbursts in Massive Young stellar objects (NAOMY)”, and Large Grant INAF 2022 “YSOs Outflows, Disks and Accretion: towards a global framework for the evolution of planet forming systems (YODA)”. Y.-L.Y. acknowledges support from Grant-in-Aid from the Ministry of Education, Culture, Sports, Science, and Technology of Japan (20H05845, 20H05844, 22K20389), and a pioneering project in RIKEN (Evolution of Matter in the Universe). RK acknowledges financial support via the Heisenberg Research Grant funded by the Deutsche Forschungsgemeinschaft (DFG, German Research Foundation) under grant no. KU 2849/9, project no. 445783058. NJE thanks the Astronomy Department of the University of Texas for research support. S.J.W. acknowledges support from the Smithsonian Institution and the Chandra X-ray Center through NASA contract NAS8-03060.

Facility: JWST (NIRSpec, MIRI), ALMA

© 2025. All rights reserved

REFERENCES

Aso, Y., Kwon, W., Ohashi, N., et al. 2023, ApJ, 954, 101, doi: [10.3847/1538-4357/ace624](https://doi.org/10.3847/1538-4357/ace624)

Barsony, M., Wolf-Chase, G. A., Ciardi, D. R., & O’Linger, J. 2010, ApJ, 720, 64, doi: [10.1088/0004-637X/720/1/64](https://doi.org/10.1088/0004-637X/720/1/64)

Beltrán, M. T., & de Wit, W. J. 2016, A&A Rv, 24, 6, doi: [10.1007/s00159-015-0089-z](https://doi.org/10.1007/s00159-015-0089-z)

Böker, T., Arribas, S., Lützgendorf, N., et al. 2022, A&A, 661, A82, doi: [10.1051/0004-6361/202142589](https://doi.org/10.1051/0004-6361/202142589)

Boogert, A. C. A., Gerakines, P. A., & Whittet, D. C. B. 2015, ARA&A, 53, 541, doi: [10.1146/annurev-astro-082214-122348](https://doi.org/10.1146/annurev-astro-082214-122348)

Bourke, T. L., Crapsi, A., Myers, P. C., et al. 2005, ApJL, 633, L129, doi: [10.1086/498449](https://doi.org/10.1086/498449)

Bourke, T. L., Myers, P. C., Evans, Neal J., I., et al. 2006, ApJL, 649, L37, doi: [10.1086/508161](https://doi.org/10.1086/508161)

Brunken, N. G. C., Rocha, W. R. M., van Dishoeck, E. F., et al. 2024, *A&A*, 685, A27, doi: [10.1051/0004-6361/202348718](https://doi.org/10.1051/0004-6361/202348718)

Bushouse, H., Eisenhamer, J., Dencheva, N., et al. 2023a, JWST Calibration Pipeline, 1.9.5, Zenodo, doi: [10.5281/zenodo.7692609](https://doi.org/10.5281/zenodo.7692609)

—. 2023b, JWST Calibration Pipeline, 1.11.3, Zenodo, doi: [10.5281/zenodo.8157276](https://doi.org/10.5281/zenodo.8157276)

Cabrit, S., Ferreira, J., & Raga, A. C. 1999, *A&A*, 343, L61

Caratti o Garatti, A., Ray, T. P., Kavanagh, P. J., et al. 2024, *A&A*, 691, A134, doi: [10.1051/0004-6361/202451350](https://doi.org/10.1051/0004-6361/202451350)

de Valon, A., Dougados, C., Cabrit, S., et al. 2022, *A&A*, 668, A78, doi: [10.1051/0004-6361/202141316](https://doi.org/10.1051/0004-6361/202141316)

Delabrosse, V., Dougados, C., Cabrit, S., et al. 2024, *A&A*, 688, A173, doi: [10.1051/0004-6361/202449176](https://doi.org/10.1051/0004-6361/202449176)

di Francesco, J., Evans, N. J., I., Caselli, P., et al. 2007, in *Protostars and Planets V*, ed. B. Reipurth, D. Jewitt, & K. Keil, 17, doi: [10.48550/arXiv.astro-ph/0602379](https://doi.org/10.48550/arXiv.astro-ph/0602379)

Diaz-Rodriguez, A. K., Anglada, G., Blázquez-Calero, G., et al. 2022, *ApJ*, 930, 91, doi: [10.3847/1538-4357/ac3b50](https://doi.org/10.3847/1538-4357/ac3b50)

Dunham, M. M., Crapsi, A., Evans, II, N. J., et al. 2008, *ApJS*, 179, 249, doi: [10.1086/591085](https://doi.org/10.1086/591085)

Dunham, M. M., Stephens, I. W., Myers, P. C., et al. 2024, *MNRAS*, 533, 3828, doi: [10.1093/mnras/stae2018](https://doi.org/10.1093/mnras/stae2018)

Dunham, M. M., Evans, Neal J., I., Bourke, T. L., et al. 2006, *ApJ*, 651, 945, doi: [10.1086/508051](https://doi.org/10.1086/508051)

Dunham, M. M., Stutz, A. M., Allen, L. E., et al. 2014, in *Protostars and Planets VI*, ed. H. Beuther, R. S. Klessen, C. P. Dullemond, & T. Henning, 195–218, doi: [10.2458/azu_uapress_9780816531240-ch009](https://doi.org/10.2458/azu_uapress_9780816531240-ch009)

Federman, S., Megeath, S. T., Tobin, J. J., et al. 2023, *ApJ*, 944, 49, doi: [10.3847/1538-4357/ac9f4b](https://doi.org/10.3847/1538-4357/ac9f4b)

Federman, S. A., Megeath, S. T., Rubinstein, A. E., et al. 2024, *ApJ*, 966, 41, doi: [10.3847/1538-4357/ad2fa0](https://doi.org/10.3847/1538-4357/ad2fa0)

Federman, S. A., Megeath, S. T., Garatti, A. C. o., et al. 2026, arXiv e-prints, arXiv:2601.09587, doi: [10.48550/arXiv.2601.09587](https://doi.org/10.48550/arXiv.2601.09587)

Federrath, C., Schrön, M., Banerjee, R., & Klessen, R. S. 2014, *ApJ*, 790, 128, doi: [10.1088/0004-637X/790/2/128](https://doi.org/10.1088/0004-637X/790/2/128)

Feeney-Johansson, A., Aikawa, Y., Takakuwa, S., et al. 2025, arXiv e-prints, arXiv:2512.21454. <https://arxiv.org/abs/2512.21454>

Fischer, W. J., Hillenbrand, L. A., Herczeg, G. J., et al. 2023, in *Astronomical Society of the Pacific Conference Series*, Vol. 534, *Protostars and Planets VII*, ed. S. Inutsuka, Y. Aikawa, T. Muto, K. Tomida, & M. Tamura, 355, doi: [10.48550/arXiv.2203.11257](https://doi.org/10.48550/arXiv.2203.11257)

Fischer, W. J., Megeath, S. T., Furlan, E., et al. 2017, *ApJ*, 840, 69, doi: [10.3847/1538-4357/aa6d69](https://doi.org/10.3847/1538-4357/aa6d69)

Gordon, I. E., Rothman, L. S., Hargreaves, R. J., et al. 2022, *JQSRT*, 277, 107949, doi: [10.1016/j.jqsrt.2021.107949](https://doi.org/10.1016/j.jqsrt.2021.107949)

Guszejnov, D., Grudić, M. Y., Offner, S. S. R., et al. 2022, *MNRAS*, 515, 4929, doi: [10.1093/mnras/stac2060](https://doi.org/10.1093/mnras/stac2060)

Guszejnov, D., Hopkins, P. F., Grudić, M. Y., Krumholz, M. R., & Federrath, C. 2018, *MNRAS*, 480, 182, doi: [10.1093/mnras/sty1847](https://doi.org/10.1093/mnras/sty1847)

Habel, N. M., Megeath, S. T., Booker, J. J., et al. 2021, *ApJ*, 911, 153, doi: [10.3847/1538-4357/abded8](https://doi.org/10.3847/1538-4357/abded8)

Hartmann, L., Herczeg, G., & Calvet, N. 2016, *ARA&A*, 54, 135, doi: [10.1146/annurev-astro-081915-023347](https://doi.org/10.1146/annurev-astro-081915-023347)

Hennebelle, P., & Grudić, M. Y. 2024, *ARA&A*, 62, 63, doi: [10.1146/annurev-astro-052622-031748](https://doi.org/10.1146/annurev-astro-052622-031748)

Hsieh, C.-H., Arce, H. G., Li, Z.-Y., et al. 2023, *ApJ*, 947, 25, doi: [10.3847/1538-4357/acba13](https://doi.org/10.3847/1538-4357/acba13)

Hsieh, T.-H., Hirano, N., Belloche, A., et al. 2019, *ApJ*, 871, 100, doi: [10.3847/1538-4357/aaf4fe](https://doi.org/10.3847/1538-4357/aaf4fe)

Hsieh, T.-H., Lai, S.-P., Belloche, A., & Wyrowski, F. 2016, *ApJ*, 826, 68, doi: [10.3847/0004-637X/826/1/68](https://doi.org/10.3847/0004-637X/826/1/68)

Huard, T. L., Myers, P. C., Murphy, D. C., et al. 2006, *ApJ*, 640, 391, doi: [10.1086/498742](https://doi.org/10.1086/498742)

Jakobsen, P., Ferruit, P., Alves de Oliveira, C., et al. 2022, *A&A*, 661, A80, doi: [10.1051/0004-6361/202142663](https://doi.org/10.1051/0004-6361/202142663)

Khanzadyan, T., Gredel, R., Smith, M. D., & Stanke, T. 2004, *A&A*, 426, 171, doi: [10.1051/0004-6361:20041241](https://doi.org/10.1051/0004-6361:20041241)

Konigl, A., & Pudritz, R. E. 2000, in *Protostars and Planets IV*, ed. V. Mannings, A. P. Boss, & S. S. Russell, 759, doi: [10.48550/arXiv.astro-ph/9903168](https://doi.org/10.48550/arXiv.astro-ph/9903168)

Law, D. R., E. Morrison, J., Argyriou, I., et al. 2023, *AJ*, 166, 45, doi: [10.3847/1538-3881/acddd8](https://doi.org/10.3847/1538-3881/acddd8)

Law, D. R., Argyriou, I., Gordon, K. D., et al. 2024, arXiv e-prints, arXiv:2409.15435, doi: [10.48550/arXiv.2409.15435](https://doi.org/10.48550/arXiv.2409.15435)

Lee, C.-F. 2020, *A&A Rv*, 28, 1, doi: [10.1007/s00159-020-0123-7](https://doi.org/10.1007/s00159-020-0123-7)

Lee, C.-F., Tabone, B., Cabrit, S., et al. 2021, *ApJL*, 907, L41, doi: [10.3847/2041-8213/abda38](https://doi.org/10.3847/2041-8213/abda38)

Manoj, P., Green, J. D., Megeath, S. T., et al. 2016, *ApJ*, 831, 69, doi: [10.3847/0004-637X/831/1/69](https://doi.org/10.3847/0004-637X/831/1/69)

Masson, C. R., & Chernin, L. M. 1993, *ApJ*, 414, 230, doi: [10.1086/173071](https://doi.org/10.1086/173071)

Megeath, T., Anglada, G., Atnagulov, P., et al. 2021, Investigating Protostellar Accretion Across the Mass Spectrum, JWST Proposal. Cycle 1, ID. #1802

Najita, J. R., & Shu, F. H. 1994, *ApJ*, 429, 808, doi: [10.1086/174365](https://doi.org/10.1086/174365)

Nakatani, R., Rosotti, G., Tabone, B., & Sellek, A. 2025, arXiv e-prints, arXiv:2511.00515, doi: [10.48550/arXiv.2511.00515](https://doi.org/10.48550/arXiv.2511.00515)

Narang, M., Ohashi, N., Tobin, J. J., et al. 2025, arXiv e-prints, arXiv:2502.00394, doi: [10.48550/arXiv.2502.00394](https://doi.org/10.48550/arXiv.2502.00394)

Narang, M., Manoj, P., Tyagi, H., et al. 2023, *Journal of Astrophysics and Astronomy*, 44, 92, doi: [10.1007/s12036-023-09982-4](https://doi.org/10.1007/s12036-023-09982-4)

—. 2024, *ApJL*, 962, L16, doi: [10.3847/2041-8213/ad1de3](https://doi.org/10.3847/2041-8213/ad1de3)

Nazari, P., Rocha, W. R. M., Rubinstein, A. E., et al. 2024, *A&A*, 686, A71, doi: [10.1051/0004-6361/202348695](https://doi.org/10.1051/0004-6361/202348695)

Neufeld, D. A., Manoj, P., Tyagi, H., et al. 2024, arXiv e-prints, arXiv:2404.07299, doi: [10.48550/arXiv.2404.07299](https://doi.org/10.48550/arXiv.2404.07299)

Ohashi, N., Tobin, J. J., Jørgensen, J. K., et al. 2023, *ApJ*, 951, 8, doi: [10.3847/1538-4357/acd384](https://doi.org/10.3847/1538-4357/acd384)

Oliva, A., & Kuiper, R. 2023, *A&A*, 669, A81, doi: [10.1051/0004-6361/202244434](https://doi.org/10.1051/0004-6361/202244434)

Ostriker, E. C., Lee, C.-F., Stone, J. M., & Mundy, L. G. 2001, *ApJ*, 557, 443, doi: [10.1086/321649](https://doi.org/10.1086/321649)

Panoglou, D., Cabrit, S., Pineau Des Forêts, G., et al. 2012, *A&A*, 538, A2, doi: [10.1051/0004-6361/200912861](https://doi.org/10.1051/0004-6361/200912861)

Pascucci, I., Cabrit, S., Edwards, S., et al. 2023, in *Astronomical Society of the Pacific Conference Series*, Vol. 534, *Protostars and Planets VII*, ed. S. Inutsuka, Y. Aikawa, T. Muto, K. Tomida, & M. Tamura, 567, doi: [10.48550/arXiv.2203.10068](https://doi.org/10.48550/arXiv.2203.10068)

Pascucci, I., Beck, T. L., Cabrit, S., et al. 2025, *Nature Astronomy*, 9, 81, doi: [10.1038/s41550-024-02385-7](https://doi.org/10.1038/s41550-024-02385-7)

Pokhrel, R., Megeath, S. T., Gutermuth, R. A., et al. 2023, *ApJS*, 266, 32, doi: [10.3847/1538-4365/acbfac](https://doi.org/10.3847/1538-4365/acbfac)

Pontoppidan, K. M., Evans, N., Bergner, J., & Yang, Y.-L. 2024, *Research Notes of the American Astronomical Society*, 8, 68, doi: [10.3847/2515-5172/ad303f](https://doi.org/10.3847/2515-5172/ad303f)

Pudritz, R. E., & Norman, C. A. 1983, *ApJ*, 274, 677, doi: [10.1086/161481](https://doi.org/10.1086/161481)

—. 1986, *ApJ*, 301, 571, doi: [10.1086/163924](https://doi.org/10.1086/163924)

Pudritz, R. E., Ouyed, R., Fendt, C., & Brandenburg, A. 2007, in *Protostars and Planets V*, ed. B. Reipurth, D. Jewitt, & K. Keil, 277, doi: [10.48550/arXiv.astro-ph/0603592](https://doi.org/10.48550/arXiv.astro-ph/0603592)

Pudritz, R. E., & Ray, T. P. 2019, *Frontiers in Astronomy and Space Sciences*, 6, 54, doi: [10.3389/fspas.2019.00054](https://doi.org/10.3389/fspas.2019.00054)

Rabenanahary, M., Cabrit, S., Meliani, Z., & Pineau des Forêts, G. 2022, *A&A*, 664, A118, doi: [10.1051/0004-6361/202243139](https://doi.org/10.1051/0004-6361/202243139)

Raga, A., & Cabrit, S. 1993, *A&A*, 278, 267

Ray, T. P., & Ferreira, J. 2021, *NewAR*, 93, 101615, doi: [10.1016/j.newar.2021.101615](https://doi.org/10.1016/j.newar.2021.101615)

Ray, T. P., Mundt, R., Dyson, J. E., Falle, S. A. E. G., & Raga, A. C. 1996, *ApJL*, 468, L103, doi: [10.1086/310239](https://doi.org/10.1086/310239)

Rieke, G. H., Wright, G. S., Böker, T., et al. 2015, *PASP*, 127, 584, doi: [10.1086/682252](https://doi.org/10.1086/682252)

Rivera-Ortiz, P. R., de A. Schutze, A., Lefloch, B., & Gusdorf, A. 2023, *A&A*, 672, A116, doi: [10.1051/0004-6361/202245085](https://doi.org/10.1051/0004-6361/202245085)

Rubinstein, A. E., Evans, N. J., Tyagi, H., et al. 2024, *ApJ*, 974, 112, doi: [10.3847/1538-4357/ad6b92](https://doi.org/10.3847/1538-4357/ad6b92)

Shang, H., Krasnopolsky, R., & Liu, C.-F. 2023a, *ApJL*, 945, L1, doi: [10.3847/2041-8213/acaee](https://doi.org/10.3847/2041-8213/acaee)

Shang, H., Krasnopolsky, R., Liu, C.-F., & Wang, L.-Y. 2020, *ApJ*, 905, 116, doi: [10.3847/1538-4357/abbdb0](https://doi.org/10.3847/1538-4357/abbdb0)

Shang, H., Li, Z. Y., & Hirano, N. 2007, in *Protostars and Planets V*, ed. B. Reipurth, D. Jewitt, & K. Keil, 261

Shang, H., Liu, C.-F., Krasnopolsky, R., & Wang, L.-Y. 2023b, *ApJ*, 944, 230, doi: [10.3847/1538-4357/aca763](https://doi.org/10.3847/1538-4357/aca763)

Sharma, R., Jørgensen, J. K., van 't Hoff, M. L. R., et al. 2025, arXiv e-prints, arXiv:2509.19158, <https://arxiv.org/abs/2509.19158>

Shu, F., Najita, J., Ostriker, E., et al. 1994, *ApJ*, 429, 781, doi: [10.1086/174363](https://doi.org/10.1086/174363)

Slaviceńska, K., van Dishoeck, E. F., Tychoniec, L., et al. 2024, *A&A*, 688, A29, doi: [10.1051/0004-6361/202449785](https://doi.org/10.1051/0004-6361/202449785)

Stanke, T., Smith, M. D., Gredel, R., & Khanzadyan, T. 2006, *A&A*, 447, 609, doi: [10.1051/0004-6361:20041331](https://doi.org/10.1051/0004-6361:20041331)

Tabone, B., Raga, A., Cabrit, S., & Pineau des Forêts, G. 2018, *A&A*, 614, A119, doi: [10.1051/0004-6361/201732031](https://doi.org/10.1051/0004-6361/201732031)

Tabone, B., Rosotti, G. P., Cridland, A. J., Armitage, P. J., & Lodato, G. 2022, *MNRAS*, 512, 2290, doi: [10.1093/mnras/stab3442](https://doi.org/10.1093/mnras/stab3442)

Tobin, J. J., & Sheehan, P. D. 2024, *ARA&A*, 62, 203, doi: [10.1146/annurev-astro-052920-103752](https://doi.org/10.1146/annurev-astro-052920-103752)

Tobin, J. J., Hartmann, L., Chiang, H.-F., et al. 2011, *ApJ*, 740, 45, doi: [10.1088/0004-637X/740/1/45](https://doi.org/10.1088/0004-637X/740/1/45)

Tyagi, H., Manoj, P., Narang, M., et al. 2024, arXiv e-prints, arXiv:2410.06697, doi: [10.48550/arXiv.2410.06697](https://doi.org/10.48550/arXiv.2410.06697)

Tychoniec, L., van Gelder, M. L., van Dishoeck, E. F., et al. 2024, *A&A*, 687, A36, doi: [10.1051/0004-6361/202348889](https://doi.org/10.1051/0004-6361/202348889)

Wang, L., Bai, X.-N., & Goodman, J. 2019, *ApJ*, 874, 90, doi: [10.3847/1538-4357/ab06fd](https://doi.org/10.3847/1538-4357/ab06fd)

Wang, L., & Goodman, J. 2017, *ApJ*, 847, 11, doi: [10.3847/1538-4357/aa8726](https://doi.org/10.3847/1538-4357/aa8726)

Wardle, M., & Koenigl, A. 1993, *ApJ*, 410, 218, doi: [10.1086/172739](https://doi.org/10.1086/172739)

Watson, D. M., Calvet, N. P., Fischer, W. J., et al. 2016, *ApJ*, 828, 52, doi: [10.3847/0004-637X/828/1/52](https://doi.org/10.3847/0004-637X/828/1/52)

Watson, D. M., Narang, M., Pittman, C. V., et al. 2025, arXiv e-prints, arXiv:2512.15999, doi: [10.48550/arXiv.2512.15999](https://doi.org/10.48550/arXiv.2512.15999)

Weintraub, D. A., Kastner, J. H., & Whitney, B. A. 1995, ApJL, 452, L141, doi: [10.1086/309720](https://doi.org/10.1086/309720)

Wright, G. S., Wright, D., Goodson, G. B., et al. 2015, PASP, 127, 595, doi: [10.1086/682253](https://doi.org/10.1086/682253)

Wright, G. S., Rieke, G. H., Glasse, A., et al. 2023, PASP, 135, 048003, doi: [10.1088/1538-3873/acbe66](https://doi.org/10.1088/1538-3873/acbe66)

Yen, H.-W., Koch, P. M., Takakuwa, S., et al. 2017, ApJ, 834, 178, doi: [10.3847/1538-4357/834/2/178](https://doi.org/10.3847/1538-4357/834/2/178)

Yen, H.-W., Williams, J. P., Sai, J., et al. 2024, ApJ, 969, 125, doi: [10.3847/1538-4357/ad4c6b](https://doi.org/10.3847/1538-4357/ad4c6b)

Young, C. H., Jørgensen, J. K., Shirley, Y. L., et al. 2004, ApJS, 154, 396, doi: [10.1086/422818](https://doi.org/10.1086/422818)

Zucker, C., Speagle, J. S., Schlafly, E. F., et al. 2020, A&A, 633, A51, doi: [10.1051/0004-6361/201936145](https://doi.org/10.1051/0004-6361/201936145)